

pubs.acs.org/JACS Article

# Direct Probe of Conical Intersection Photochemistry by Time-Resolved X-ray Magnetic Circular Dichroism

Shichao Sun,\* Bing Gu, Hang Hu, Lixin Lu, Diandong Tang, Vladimir Y. Chernyak, Xiaosong Li,\* and Shaul Mukamel\*



Cite This: J. Am. Chem. Soc. 2024, 146, 19863-19873



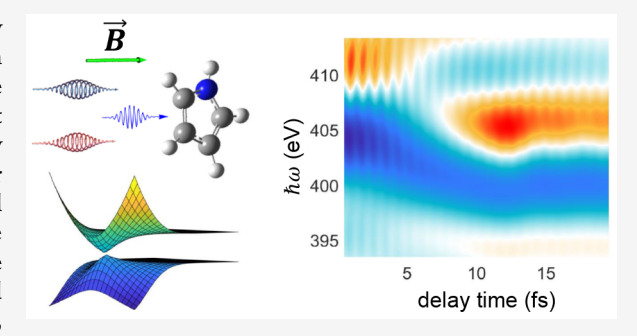
**ACCESS** 

III Metrics & More

Article Recommendations

s Supporting Information

ABSTRACT: The direct probing of photochemical dynamics by detecting the electronic coherence generated during passage through conical intersections is an intriguing challenge. The weak coherence signal and the difficulty in preparing purely excited wave packets that exclude coherence from other sources make it experimentally challenging. We propose to use time-resolved X-ray magnetic circular dichroism to probe the wave packet dynamics around the conical intersection. The magnetic field amplifies the relative strength of the electronic coherence signal compared to populations through the magnetic field response anisotropy. More importantly, since the excited state relaxation through conical intersections involves a change of parity, the magnetic coupling matches the symmetry of the response function



with the electronic coherence, making the coherence signal only sensitive to the conical intersection induced coherence and excludes the pump pulse induced coherence between the ground state and excited state. In this theoretical study, we apply this technique to the photodissociation dynamics of a pyrrole molecule and demonstrate its capability of probing electronic coherence at a conical intersection as well as population transfer. We demonstrate that a magnetic field can be effectively used to extract novel information about electron and nuclear molecular dynamics.

## ■ INTRODUCTION

Photochemical processes play a pivotal role in a wide array of fields including photocatalysis, solar energy conversion, environmental remediation, biophysics, and organic synthesis. The study of photochemical energy transfer pathways, particularly during excited state relaxation and decoherence, is of fundamental interest. These advancements are key in various applications to green chemistry, artificial photosynthesis, and the efficient production of fuels and valuable chemicals. Understanding photochemical processes involving the passage through conical intersections (CoIn) is crucial, as they are the dominant pathways for excited state relaxation in photochemical reaction mechanisms.

Ultrafast pump—probe spectroscopy is a powerful tool for monitoring photoinduced molecular processes. <sup>14,15</sup> In this technique, a broadband pump light pulse creates a superposition of vibronic states, thereby launching a wave packet dynamics. A probe pulse with variable time delay subsequently interacts with the wave packet, going through stimulated emission, ground state bleaching, or excited state absorption pathways <sup>16</sup> and producing spectroscopic signature of the dynamics, including vibronic state coherences, state-to-state population transfer, relaxation, and decoherences.

Probing CoIn, especially the electronic coherence generated at CoIn with pump-probe spectroscopy has been studied

experimentally and theoretically by transient absorption, <sup>17</sup> time-resolved X-ray diffraction, <sup>18–20</sup> and time-resolved photo-electron spectroscopy (tr-PES). <sup>21,22</sup> Transient absorption can detect wave packet transfer between states, providing an indirect evidence of conical intersections. <sup>23</sup> The direct observation of conical intersection signatures throughout the wave packet dynamics remains an experimental challenge. Transient redistribution of ultrafast electronic coherence in attosecond Raman signals (TRUECARS) is specifically designed to detect the electronic state coherence generated when the wave packet passes through the conical intersection. <sup>24–27</sup>

In this theoretical study, we propose time-resolved X-ray magnetic circular dichroism (tr-XMCD) to observe the excited state relaxation and the signatures of electronic coherence generated at conical intersections. MCD is the differential absorption of left and right circularly polarized light by a sample subjected to a uniform magnetic field parallel to the

Received: February 29, 2024 Revised: June 13, 2024 Accepted: June 14, 2024 Published: July 11, 2024





direction of the incident light's propagation.<sup>28-30</sup> In this proposed tr-XMCD, the dynamics of molecule is initiated by a UV-visible pump and probed with attosecond circularly polarized X-ray pulses<sup>31–40</sup> in a uniform magnetic field. We demonstrate that tr-XMCD can effectively detect the electronic coherences generated at CoIn. When we have a coherent superposition of states with well-defined relative phases and amplitudes, the cross terms of different states are known as coherence. For example, vibronic coherence is the cross term of vibronic states, which are the eigen states of the total nuclear and electronic molecular Hamiltonian, while electronic coherence is the cross term of electronic states, which are the eigen states of electronic Hamiltonian. At conical intersections, the electronic coherences are generated when the wave packet partially transfers between electronic states. It is usually difficult to observe these coherences in conventional transient absorption spectroscopy, as they are weak and buried in the population signal. In tr-XMCD, in contrast, the magneto optical response amplifies the relative strength of the coherence signal compared to the population part by making the two comparable through anisotropic magnetic coupling and the change of spatial symmetry in the response function. tr-XMCD thus provides a clear spectroscopic signature of conical intersections. Additionally, tr-XMCD only probes the electronic coherence generated at CoIn but excludes the electronic coherence produced by the pump pulse, since the latter possess a different symmetry from the magnetic optical response in the XMCD signal. The preparation of the excited states is greatly simplified since it does not require bringing the entire wave packet to the excited state to exclude pumpinduced electronic coherence, like in TRUECARS.<sup>24</sup>

Although the perturbative effect of the magnetic field is weak on the atomic scale, probing the MCD in the X-ray frequency regime for rotationally averaged sample is still much easier than natural circular dichroism (NCD), <sup>28,41-43</sup> since MCD stems from electric dipole-electric dipole interference in the presence of a magnetic field, 28 while NCD is the electric dipolemagnetic dipole interference, where the transition magnetic dipole between core-shell and valence shell is especially weak.<sup>28,41-43</sup> Additionally, MCD probes both chiral and achiral molecules<sup>29,30,44-48</sup> while NCD only probes chiral molecules.

XMCD<sup>41,49,50</sup> has thus been employed to investigate the magnetization of transition metal and rare earth elements in solid state materials, 51-57 as well as to detect the spin state and structural characteristics of transition metal ions in clusters and molecules.<sup>58-61</sup> tr-XMCD at the transition metal L-edge has been utilized to track photoinduced magnetization and the evolution of spin and orbital angular momentum in solid state transition metal alloys, 62-65 down to the femtosecond time scale, 66,67 where the orbital and spin angular momentum are evaluated through the L-edge sum rules. 68-72 The proposed experiment extends the tr-XMCD technique to the liquid and gas phase in order to probe the nonadiabatic wave packet dynamics in molecular systems initiated by a pump pulse, focusing on the processes occurring in the vicinity of conical intersections. It provides a clear signature of the electronic coherence generated at the CoIn. Additionally, as the XMCD signal scales linearly with the magnetic field magnitude, we anticipate that advancements in strong magnetic fields will significantly enhance the accuracy and sensitivity of tr-XMCD.<sup>73-7</sup>

#### RESULTS AND DISCUSSION

Application to Bond Dissociation in Pyrrole. We demonstrate the tr-XMCD signals for photodissociation of the pyrrole molecule. Pyrrole and its derivatives have significant pharmaceutical applications<sup>79</sup> and play a crucial role in DNA sequence recognition.<sup>80,81</sup> An understanding of pyrrole's photochemistry is relevant to many biochemical processes.<sup>82</sup> Additionally, as a heterocyclic aromatic molecule, its anisotropic magnetic response, where diamagnetic ring currents are produced in the molecule with perpendicular magnetic fields, can amplify the coherent tr-XMCD signal produced during the wave packet passage through CoIn. Besides, the nitrogen atom connected directly to the dissociating H atom is used as an X-ray chromophore, making the X-ray signal particularly sensitive to the dissociation dynamics. However, the MCD signal of pyrrole originates from the B-term, <sup>29</sup> caused by the mixing of states through magnetic perturbation. Stronger MCD signals can be produced from molecular systems with excited state or spin degeneracy, which produce A-term and C-term, respectively, induced by orbitaland spin-Zeeman effects.

Figure 1 illustrates the photodissociation pathway of pyrrole. The three spin-singlet valence states  $A_1$ ,  $A_2(\pi\sigma^*)$ , and  $B_1(\pi\sigma^*)$ states are labeled in energy ascending order at the Frank-Condon point as  $\tilde{X}$ ,  $\tilde{A}$ , and  $\tilde{B}$ .  $\tilde{A}$  and  $\tilde{B}$  are  $\pi - \sigma^*$  excitations, where the electron in the conjugated  $\pi$  orbital (a2 and b1 orbitals respectively) is excited to N-H  $\sigma$ -antibonding orbital with 3s Rydberg feature.  $\tilde{A}$  and  $\tilde{B}$  intersect with  $\tilde{X}$  at  $r_{\rm N-H} \approx 2.1$ and 2.2 Å, respectively, but do not intersect with each other. Upon excitation to the  $\tilde{B}$  state, the N-H bond begins to stretch, eventually leading to dissociation as the wave function relaxes to the ground state  $(\tilde{X})$  in 20 fs.<sup>83</sup> This ultrafast nonadiabatic dynamics is driven by the efficient relaxation pathway involving the  $\tilde{B}-\tilde{X}$  conical intersection around  $r \approx$ 3.35 Å  $(r_{N-H} \approx 2.2 \text{ Å})$  with strong nonadiabatic coupling involving the H out of plane bending motion. A portion of the  $ilde{B}$  wave packet relaxes to  $ilde{A}$  though a relatively weaker nonadiabatic coupling with a vibrational mode of the C<sub>4</sub>H<sub>4</sub>N ring. This photodissociation process has been previously simulated using exact nonadiabatic wave packet dynamics8 with a vibronic model that incorporates X and B electronic states and two nuclear Jacobi coordinates: the stretching (r,distance between the dissociating H and the remaining C<sub>4</sub>H<sub>4</sub>N group center of mass) and the out-of-plane bending of the dissociating H coordinate  $(\gamma)$ , as depicted in Figure 1a. We selected these two vibrational degrees of freedom in the wave packet dynamics simulation (see the "Methods" section). The following illustrative simulation of the tr-XMCD spectra aims at demonstrating its capability to detect conical intersection. The B to A relaxation pathway is not considered in the dynamics simulation, as the nitrogen K-edge excitation from the A state has no contribution to the signal in the 395–410 eV energy regime.

The wave packet evolves with time according to the Schrödinger equation. Snapshots of the wave packet dynamics given by Jacobi coordinates r and  $\gamma$  at different time delays are presented in Figure 2. The dynamics begins at the Franck-Condon point (r = 2.05 Å, or  $r_{N-H} = 0.9 \text{ Å}$ ) on the B surface at T = 0 fs, with the majority of the population initially on  $\tilde{B}$ , though a small amount begins to appear on  $\tilde{X}$  as the wave packet evolves. By T = 10 fs, the wave packet approaches the B-X conical intersection at r=3.35 Å ( $r_{N-H}=2.2$  Å). At this

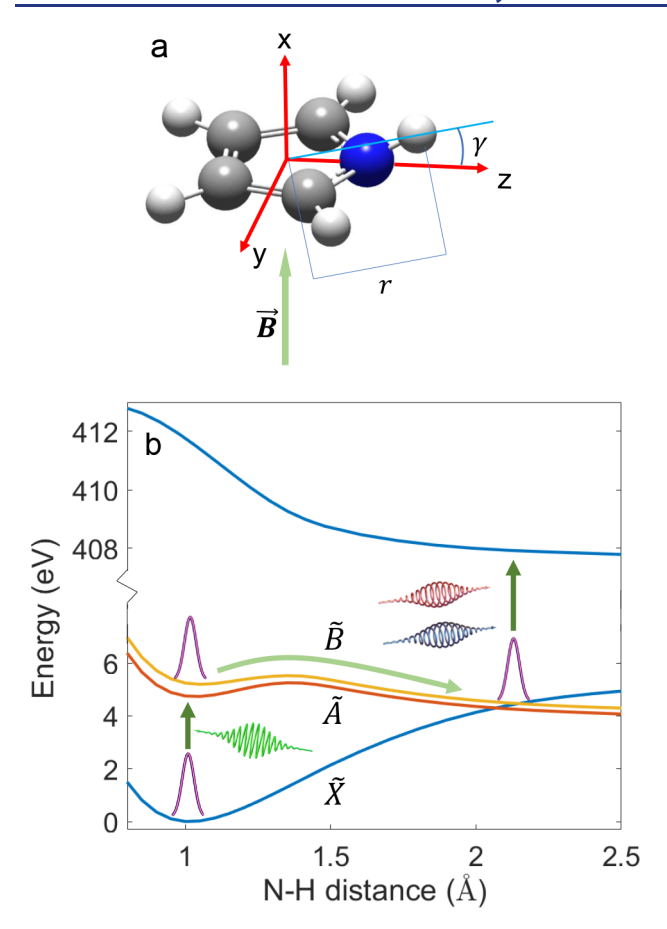


**Figure 1.** a. Jacobi coordinate system in the pyrrole molecule. r is the distance between the dissociating H and the remaining C<sub>4</sub>H<sub>4</sub>N group center of mass.  $\gamma$  is the angle between the center of mass-H line and the z axis. It describes the out of plane bending of H. b. Sketch of the pump probe experiment. A constant uniform magnetic field is applied to the molecular system. The dissociation of pyrrole is initiated by a UV-visible pump pulse (the green wave). As the molecule evolves, the circularly polarized X-ray probe pulses are applied to interrogate the molecule at various time delay T. Red and blue wave denote left and right circularly polarized light. Their differential spectra are measured to give X-ray magnetic circular dichroism spectra.

point, the wave packet's population is nearly evenly split between  $\tilde{B}$  and  $\tilde{X}$ . As the dynamics proceeds through the conical intersection, there is noticeable population transfer from B to X, occurring simultaneously with the bond dissociation event in both electronic states.

The  $\chi_{\tilde{x}}$  nuclear wave packet shown in Figure 2 is odd with respect to the H atom out of plane bending motion  $(\gamma)$ , while  $\chi_{\tilde{B}}$  is even. On  $\tilde{B}$ , the wave packet has quantum number  $\nu = 0$ for the bending motion. As it relaxes from the  $\tilde{B}$  state via the conical intersection, it generates the X wave packet. The presence of a geometric phase at the conical intersection leads to a distinct parity in the  $\tilde{X}$  wave packet compared to its  $\tilde{B}$ counterpart, arising from the bending motion's quantum number transitioning from 0 to 1.84 The nodal characteristics observed in the X wave packet can be thus attributed to the geometric phase that manifests near a conical intersection.<sup>85</sup>

Time-Resolved X-ray Magnetic Circular Dichroism Signal. To directly observe the wave packet dynamics traversing through the  $\tilde{B}-\tilde{X}$  conical intersection, we focus on tr-XMCD at the nitrogen K-edge, where the nitrogen 1s electron is excited to valence orbitals by circularly polarized

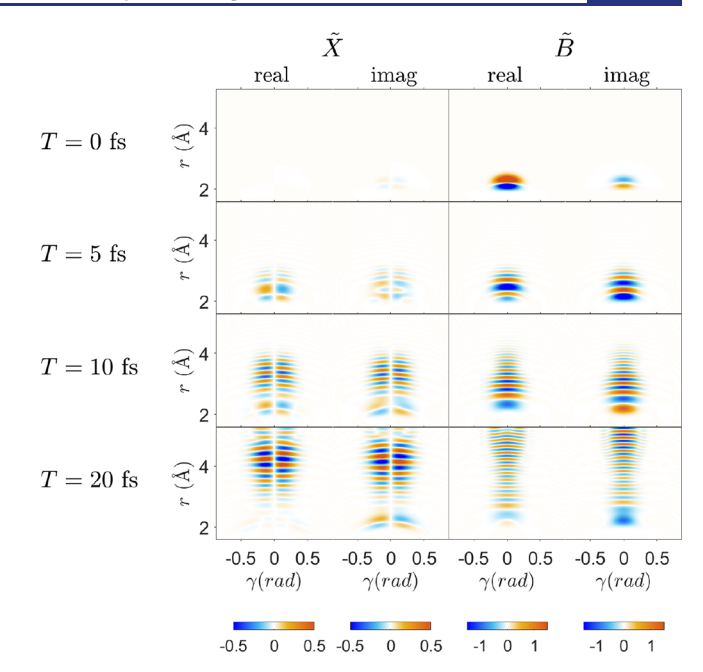


Figure 2. Wave packet of states  $\tilde{X}$  and  $\tilde{B}$  displayed in two Jacobi coordinates r and  $\gamma$  at T=0, 5, 10, and 20 fs, respectively. y axis is Jacobi coordinate r and x is  $\gamma$ . In each row, the first and second columns are the real and imaginary parts of  $\tilde{X}$  wave packet, respectively, while the third and fourth columns are the real and imaginary part of  $\tilde{B}$  wave packet, respectively. The  $\tilde{X}$  wave packet is odd with respect to bending coordinate  $\gamma$ , while B is even. The wave packet dynamics was simulated without magnetic field, since the change in energy caused by magnetic field is weak.

light pulse in the presence of a static magnetic field during the pump initiated dynamics as depicted in Figure 1, measuring the differential absorption spectra of the nitrogen K-edge at various time delays T between the pump and probe pulses, thereby generating the tr-XMCD spectrum.

We define the Cartesian coordinate frame as displayed in Figure 1a for pyrrole, where the C<sub>4</sub>H<sub>4</sub>N group is in the yz plane while the x axis is perpendicular. The indices i, j,  $k \in \{x, y\}$ y, and z are defined such that their unit vectors  $\epsilon_i$ ,  $\epsilon_i$ , and  $\epsilon_k$ form a right-handed Cartesian coordinate system. The magnetic field applied along  $\epsilon_k$  coincides with the circularly polarized pulse propagation direction. The circularly polarized probe pulse electric field has a Gaussian envelope

$$\mathbf{E}_{\pm}(t) = E_0 e^{-(t-T)^2/2\sigma^2} (\epsilon_i \sin \omega_c (t-T))$$

$$\mp \epsilon_j \cos \omega_c (t-T))$$
(1)

where  $E_0$  is the pulse amplitude,  $\omega_c$  is the pulse central frequency, and  $\sigma$  is the pulse duration. The total Hamiltonian is composed of molecular Hamiltonian eq 6 which includes the molecule-magnetic field interaction, the pump, and the probe pulse interaction.

The tr-XMCD pump-probe signal is the magneto-optical response derived in Supporting Information S1, S2 using timedependent perturbation in the light-matter electric dipole interaction. The signal can be measured with a photon counting detector. In the impulsive limit, the tr-XMCD signal of molecule with magnetic field in  $\epsilon_k$  direction is given as the magnetically perturbed electric dipole response,

$$S_{\text{XMCD},k}(T) = -2\pi i \sigma^2 E_0^2 \left[ \sum_{I,J \in \text{valence } C \in \text{core}} e^{-\sigma^2 (\omega_C - \omega_C)^2} \right]$$

$$\int d\mathbf{q} \, \chi_J^*(\mathbf{q}, T) (\langle J | \boldsymbol{\mu} | C \rangle \times \langle C | \boldsymbol{\mu} | I \rangle \cdot \boldsymbol{\epsilon}_k) \, \chi_I(\mathbf{q}, T) \right] \tag{2}$$

Alternatively, the time and frequency-resolved XMCD signal can be measured with a frequency resolved detector. The signal of an oriented molecule with magnetic field in  $\epsilon_k$  direction is given as

$$S_{\text{XMCD},k}(\omega, T) = \frac{1}{\pi \hbar^2} E_0 \Re$$

$$\left[ \sqrt{2\pi} \sigma(e^{-i(\omega - \omega_c)T} e^{-\sigma^2/2(\omega - \omega_c)^2}) \int_{-\infty}^{\infty} dt \ e^{i(\omega - \omega_c)t} \right]$$

$$\int_{0}^{t} d\delta \ E_0 \ e^{-(\delta - T)^2/2\sigma^2} \sum_{I,J \in \text{valence}} \sum_{C \in \text{core}} \int d\mathbf{q} \ \chi_J^*(\mathbf{q}, t)$$

$$e^{i(\omega_C - \omega_c)\delta} (\langle J | \boldsymbol{\mu} | C \rangle \times \langle C | \boldsymbol{\mu} | I \rangle \cdot \boldsymbol{\epsilon}_k) \ \chi_I(\mathbf{q}, \delta) \ e^{-\Gamma(t - \delta)} ]$$
(3)

It has time and nuclear coordinate integration of nuclear wave packet  $\chi_I(q,t)$ , probe pulse with a Gaussian envelope, and magnetically perturbed transition electric dipoles  $\langle J|\mu|C\rangle$ , where I,J are indices for the valence states, including ground state and valence excited states, while C denotes core excited states.  $\omega_C$  is the energy of the core excited states.  $\mathrm{e}^{-\Gamma(t-\delta)}$  describes the decay of core excited states, where  $\Gamma=0.093$  eV is the natural line width of the nitrogen K-edge. The magnetic field perturbation is implicitly included in the electronic states  $|I\rangle$ ,  $|J\rangle$ , and  $|C\rangle$ , which are eigen states of molecular electronic Hamiltonian containing the magnetic coupling eq 7, i.e., magnetic-field-dressed electronic wave functions. They are computed with CASSCF and CASCI using the magnetic field containing electronic Hamiltonian with Chronus Quantum software package.

Equations 2 and 3 are applied in simulating the tr-XMCD signal and probing the wave packet dynamics shown in Figure 2. Figure 3 displays the anisotropic tr-XMCD spectra of an oriented molecule where the magnetic field is applied along  $x_i$ y, z respectively. These spectra probe the nitrogen K-edge as the time delay T is varied between 0 and 20 fs. The simulation includes the two lowest nitrogen 1s core excited states,  ${}^{1}A_{1}(1s \rightarrow \sigma^{*})$  and  ${}^{1}B_{2}(1s \rightarrow \pi^{*})$ . All spectra contain a contribution from electronic population terms (terms with I = J in the summation of eq 2 and 3) and from electronic coherence (terms with  $I \neq J$ ). Although the separation into coherence and population is basis dependent, the XMCD signal that contains both coherences and populations is independent of the basis used. For convenience, we analyze the spectrum in the chosen diabatic basis.<sup>84</sup> The tr-XMCD spectra exhibit pronounced anisotropy, where the electronic coherence contribution is especially strong when the magnetic field is applied perpendicular to the molecular plane (in the xdirection) compared to the parallel configuration (in the y and z directions), which is dominated by electronic population. A perpendicular orientation (Figure 3a) shows a positive peak at 403 eV around 12 fs, which coincides with the wave packet passage through the conical intersection. This conical intersection signature peak is attributed to the electronic state coherences  $\chi_{X}^{*}\chi_{B}$  and  $\chi_{B}^{*}\chi_{X}$  on the diabatic electronic state basis. This is illustrated by separately plotting the population and coherence contributions in Supporting Information S3. As

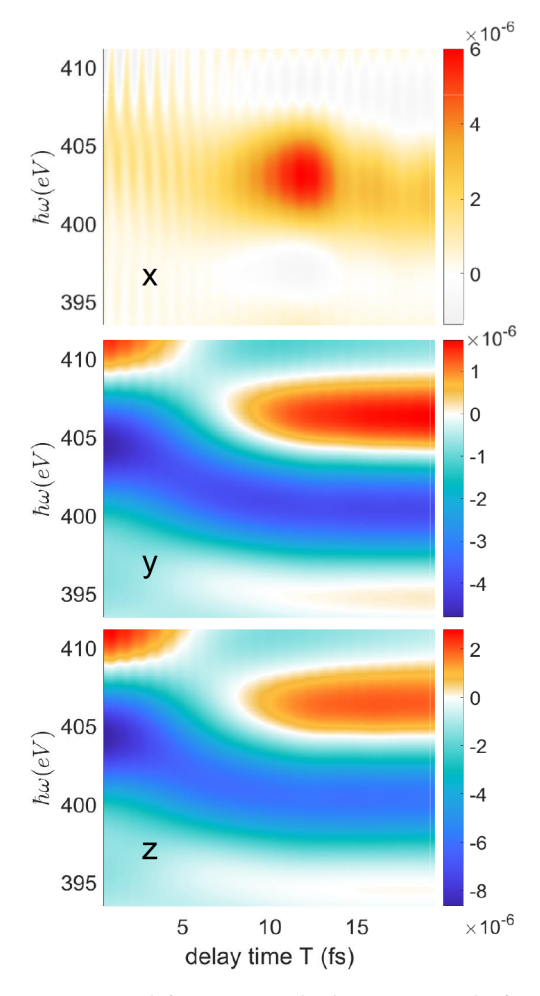


**Figure 3.** Time- and frequency-resolved XMCD signal of oriented molecule with magnetic field applied along the x, y, z direction as indicated. The X-ray probe pulse, defined in eq 1, has the central frequency  $\omega_c = 402.43$  eV, in resonance with the nitrogen K-edge absorption, and  $\sigma = 0.1$  fs. The magnitude of the magnetic field is 1 Telsa.

the wave packet gradually approaches the CoIn, it partially transfers from the excited to the ground state via the nonadiabatic coupling. The wave packet  $\chi_{\tilde{B}}$  decays, while  $\chi_{\tilde{X}}$ grows. When the excited state and ground state wave packets have comparable magnitudes, the modulus of their products reaches a maximum at the time when the wave packet passes through the conical intersection. This also makes the electronic coherence of the tr-XMCD signal reaches maximum. In other words, the maximum of the electronic coherence in tr-XMCD coincides with the passage through CoIn. The electronic coherence signal is too weak to be observed in common transient absorption, as shown in Supporting Information Figure S4. However, in tr-XMCD, the coherence signal is amplified and readily observed. The tr-XMCD technique can thus directly detect the position of the conical intersection. The amplification mechanism of the coherence signal will be explained later.

Figure 3a also exhibits 0.9 fs oscillations, indicating vibronic coherence induced by the coherent superposition of vibronic states created by the pump. Due to its weak strength, it is quickly buried in the electronic coherence signal.

The parallel orientations Figure 3b,c, in contrast, reveal a decaying negative peak at 405 eV and positive peak at 411 eV,

corresponding to the  $\tilde{B}$  population term in eq 3 (where  $I=J=\tilde{B}$ ), showing the decay of  $\tilde{B}$ . The new positive peak at 406 eV, contributed by the  $S_0$  population term in eq 3 (where  $I=J=\tilde{X}$ ), corresponds to the emergence of  $\tilde{X}$ . These characteristics are indicative of the wave packet's transition from  $\tilde{B}$  to  $\tilde{X}$ , resembling the transient-absorption spectrum Figure 4b, where the 408 eV peak ( $\tilde{B}$  population) decays and the 404 eV peak ( $\tilde{X}$  population) builds up monotonically.

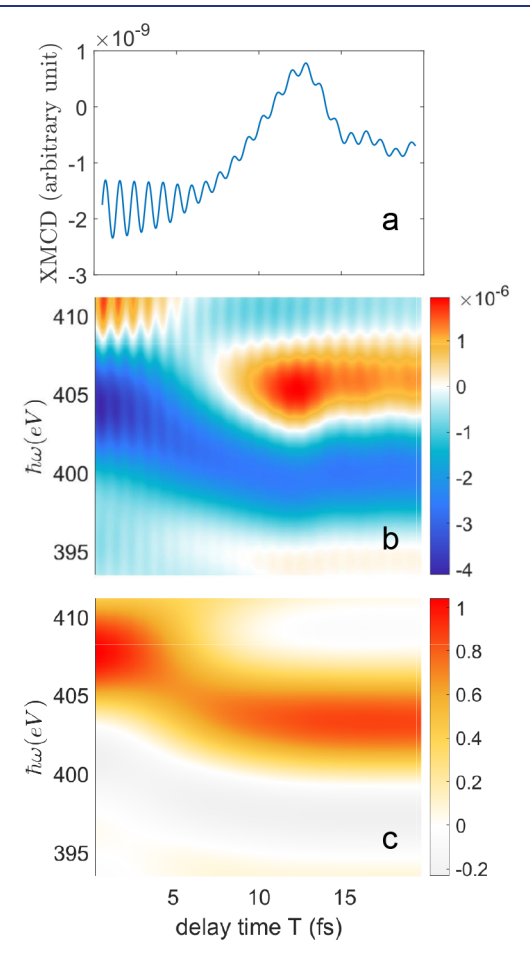


Figure 4. a. Rotationally averaged tr-XMCD signal computed with  $S_{\text{XMCD}}(T) = \frac{1}{6}(S_{\text{XMCD},x}(T) + S_{\text{XMCD},y}(T) + S_{\text{XMCD},z}(T))$  and eq 2. b. Rotationally averaged frequency and time-resolved tr-XMCD signal computed with  $S_{\text{XMCD}}(\omega, T) = \frac{1}{6}(S_{\text{XMCD},x}(\omega, T) + S_{\text{XMCD},y}(\omega, T) + S_{\text{XMCD},z}(\omega, T))$ 

.28 c. Rotationally averaged transient absorption signal. The spectrum is simulated with linearly polarized X-ray probe pulse with the central frequency  $\omega_c$  = 402.43 eV and  $\sigma$  = 0.1 fs.

The rotationally averaged time- and time-frequency-resolved tr-XMCD and ordinary transient absorption are displayed in Figure 4. The rotationally averaged tr-XMCD exhibits both perpendicular and parallel magnetic field orientation contributions. The time-resolved spectrum in Figure 4a starts with a strong negative sign, contributed by the  $\tilde{B}$  population. The coherence contribution then peaks around 12 fs, indicating the passage through the conical intersection. The pump pulse induces vibronic coherence, which causes the signal oscillation in time. In the frequency-resolved signal in Figure 4b, a bright peak at 406 eV reaches a maximum at 12 fs, constituting a unique probe of the electronic coherence generated at the

conical intersection. In contrast, the transient absorption spectrum Figure 4b is dominated by the electronic population contribution, while the coherence signal produced at the CoIn is too weak compared to the population signal to observe, as depicted in Figure S4, making the observation of CoIn hard. In Figure 4b, the  $\tilde{B}$  population peaks at 405 eV decay with time, indicating the decay of  $\tilde{B}$ . The peak at 406 eV reaches the maximum at 12 fs and then decreases and increases again, reflecting the combination of coherence and  $\tilde{X}$  population peak. This decay of excited state peaks and the emergence of ground state peaks in tr-XMCD (Figure 4b) resemble those found in traditional transient absorption Figure 4c. Although rotationally averaged tr-XMCD shows an obvious CoIn signature, the perpendicular orientation spectrum (Figure 3a) provides a clearer picture.

The amplification mechanism of electronic coherence signal in tr-XMCD boils down to two factors: (1) the magnetic perturbation alters the symmetry of electric dipole—electric dipole response function and (2) the anisotropy of magnetic response.

Altering the Electric Dipole Response Symmetry. The electronic coherence contributions in the tr-XMCD signal are observable only when the symmetry of wave packet coherence  $(\chi_I^*\chi_I)$  and signal expression  $(\mu_{IC} \times \mu_{CI} \cdot \epsilon_k)$  match, i.e., the integrand of eq  $3\chi_I^*(\mu_{IC} \times \mu_{CI} \epsilon_k)\chi_I$  contains a totally symmetric irreducible representation  $(A_1)$  in this  $C_{2\nu}$  point group, such that the integration of nuclear coordinates q in eq 3 is nonvanishing. In other words, the integrand must not be an odd function of the out of plane bending coordinate  $\gamma$ , otherwise the integration over  $\gamma$  in eq 3 vanishes. The integrand symmetry can be analyzed with irreducible representation (irrep) of the  $C_{2\nu}$  point group.<sup>88</sup> We show that for the circular dichroism signal the electronic coherence signal generated at CoIn is enabled by the coupling to the magnetic field and vanishes in its absence. Additionally, XMCD excludes the contribution from the pump pulse generated electronic coherence by symmetry.

We first find the irrep of  $\tilde{B}-\tilde{X}$  coherence. Since the conical intersection induced electronic state coherence in diabatic state basis is caused by nonadiabatic coupling in bending motion,<sup>84</sup> electronic coherence have the same irreducible representation as the bending motion (Supporting Information S4 for detail). The out of plane bending motion is mostly a motion of the H atom in the x direction, which belongs to the  $B_1$  irrep. We have the irrep of the electronic coherence  $\Gamma \chi_{S_0} \chi_{S_2} = B_1$ . In the absence of magnetic field, for probe pulse propagating in x, the integrand of eq 3 has the form of  $\chi_{\tilde{X}} \chi_{\tilde{B}}(\langle \tilde{X} | \mu_v | C \rangle \langle C | \mu_z | \tilde{B} \rangle \langle \tilde{X} | \mu_z | C \rangle \langle C | \mu_y | \tilde{B} \rangle$ ), corresponding to irrep  $\Gamma_{\tilde{X}} \otimes \Gamma_{\mu_z} \otimes \Gamma_C \otimes \Gamma_{\mu_z}$  $\Gamma_{C} \otimes \Gamma_{\mu_{y}} \otimes \Gamma_{\tilde{B}} \otimes \Gamma_{\chi_{\tilde{\chi}\chi_{\tilde{B}}}} = B_{2}$ , whose integration on the nuclear coordinate is zero. In other words, the integrand is an odd function of  $\gamma$ , resulting in zero coherence signal. In this analysis, the irrep of X and B electronic states are  $A_1$  and  $B_1$ respectively. The electric dipole operators  $\mu_x$ ,  $\mu_y$ ,  $\mu_z$  correspond to B<sub>1</sub>, B<sub>2</sub>, and A<sub>1</sub> respectively. Repeating this analysis, we find that in the absence of magnetic field, the cross term signal vanishes identically for any probe wave propatating direction, as explained in Supporting Information section S4.

In MCD, the static magnetic field is coupled with the electric dipole-electric dipole response function through a magnetic dipole operator. In  $C_{2v}$  group,  $m_x$ ,  $m_y$ ,  $m_z$  has  $B_2$ ,  $B_1$ ,  $A_2$  irreps, respectively. For the coherence contribution of MCD with magnetic field in x direction, the irrep is determined by  $\Gamma_{m_x} \otimes$ 

 $\Gamma_{\tilde{X}} \otimes \Gamma_{\mu_z} \otimes \Gamma_C \otimes \Gamma_C \otimes \Gamma_{\mu_y} \otimes \Gamma_{\tilde{B}} \otimes \Gamma_{\chi_{\tilde{X}\!X\!\tilde{B}}} = A_1$ , resulting in a nonzero coherence XMCD signal.

The assignment of the irrep of operators and wave packets is explained in detail in Supporting Information section S4. We conclude that the magnetic field alters the symmetry of electric dipole-electric dipole response  $\mu_{JC} \times \mu_{CI} \epsilon_k$  so that the electronic coherence is visible in the tr-XMCD spectrum and becomes the signature of CoIn.

The electronic coherence generated by the pump pulse makes no contribution to the tr-XMCD signal. The ground state vibrational wave function of  $\tilde{X}$  is even with respect to the bending coordinate  $\gamma$ , making its coherence with  $\chi_{\tilde{B}}$  an even function of  $\gamma$ . The product of pump induced coherence with  $\mu_{JC} \times \mu_{CI} \cdot \epsilon_k$  thus becomes an odd function of  $\gamma$ , giving zero XMCD signal. tr-XMCD can only probe the electronic coherence generated at CoIn since the passage of wave packet through CoIn involves a change of parity, while the vertical excitation by the pump maintains the wave packet parity.

The Magnetic Anisotropy. The electronic coherence of the XMCD signal is particularly strong in a perpendicular magnetic field. This XMCD signal anisotropy can be understood by magnetic field perturbation. The magnetically perturbed electric-dipole/electric-dipole response in the XMCD signal  $(\langle I|\mu |C\rangle \times \langle C|\mu |I\rangle \cdot \epsilon_k)$  in eq 3, where the magnetic field along k can be expanded to first order in the magnetic field  $^{28,89}$ 

$$\sum_{\mathring{K}} (\langle \tilde{\tilde{X}} | \boldsymbol{\mu} | \mathring{C} \rangle \times \langle \mathring{C} | \boldsymbol{\mu} | \mathring{K} \rangle)_{k} \langle \mathring{K} | m_{k} | \tilde{\tilde{X}} \rangle \frac{1}{\hbar \omega_{\mathring{K} \mathring{B}}}$$
(4)

where the terms with small contributions are ignored, as explained in Supporting Information S4. Here, we have used  $J = \tilde{X}$  and  $I = \tilde{B}$  for electronic coherence. The expression for the  $J = \tilde{B}$  and  $I = \tilde{X}$  terms is similar, and we omit it for brevity. C denotes core excited states. The circle  $^{\circ}$  indicates electronic eigenstate in the absence of a magnetic field.

Equation 4 suggests that the strength of the XMCD signal is modulated by the magnetic dipole moment  $\langle \mathring{K} | m_x | \mathring{B} \rangle$  and energy difference  $\hbar \omega_{\mathring{K} \mathring{B}}^{\circ}$ . We have computed the transition magnetic dipoles between different excited states at the Franck–Condon geometry to identify the magnetic coupling strength, as shown in Table S3. Among the computed  $\overset{\circ}{\approx}$ 

transition magnetic dipoles,  $\langle K|\mathbf{m}_x|B\rangle$  has an especially large value of -0.68i Bohr magneton. The 0.6274 eV energy gap between  $\tilde{A}-\tilde{B}$  is small. This coupling makes the electronic coherence term with a magnetic field applied along x much stronger than those aligned with y and z, giving rise to the strong anisotropy observed in the tr-XMCD spectrum.

This magnetic coupling mechanism also induces anisotropy in the ring current. When the magnetic field is perpendicular to the pyrrole molecule, a diamagnetic ring current is produced in the conjugated  $\pi$  orbital of this aromatic molecule. While for a parallel magnetic field, no ring current is produced (Figure S6).

Frequency-Resolved-Optical-Gating (FROG) Analysis. The coherence between vibronic states gives rise to oscillatory signals, encoded in the frequency dispersed spectrum, while population signals have zero frequency. To distinguish these two contributions and observe their time evolution, we integrate the tr-XMCD signal at a certain excitation energy with a temporal gate function to generate a frequency-resolved optical-gating (FROG) spectrogram

$$S_{\text{FROG}}(T, \omega') = \left| \int_{-\infty}^{\infty} dt \ S_{\text{XMCD}}(\omega, t) |_{\omega = \omega_1} E_{\text{gate}}(t - T) e^{-i\omega' t} \right|^2$$
(5)

The FROG spectrogram is essentially a Fourier transform of the tr-XMCD signal, observed within a specific time window centered at a delay time T. It reflects the oscillation frequency  $\omega'$  of the peak with energy  $\omega_1$  around delay time T. This spectrogram provides the temporal resolution necessary to observe both the population decay process and the electronic coherences generated at conical intersection, as well as the frequency resolution required to view the vibronic coherence.

Figure 5a shows the rotationally averaged FROG spectrogram at the excitation energy of  $\omega_1$  = 405.17 eV, resonant with

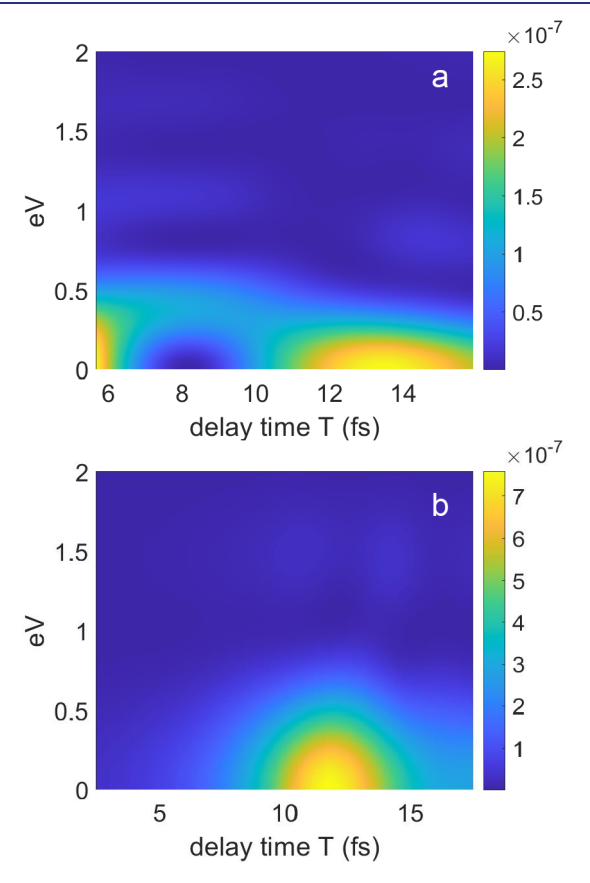


**Figure 5.** a. FROG spectrogram of the rotationally averaged tr-XMCD signal, Figure 4b with  $\omega_1$  = 405.17 eV. b. FROG spectrum of tr-XMCD signal with magnetic field applied in the  $\alpha$ direction.

the peak contributed by  $\chi_B^*\chi_B^*$  in Figure 4a. We employed a rectangular gate function with a 7.2 fs duration to obtain good spectral and temporal resolution. Initially, a faint coherence peak at  $\omega=0.4$  eV shows up, attributable to vibronic coherence induced by the coherent pump excitation. A strong zero frequency peak contributed by the  $\tilde{B}$  population is present from the beginning. This population peak fades and vanishes within 6 fs, marking relaxation of the  $\tilde{B}$  state. From 10 fs onward, a new peak with  $\omega'=0$  emerges, visible in the lower middle and right sections of Figure 5a, indicating the appearance of the  $\tilde{X}$  state. In Figure 5b, with the magnetic field applied along x, we set  $\omega=401.64$  eV to be resonant with the conical intersection signature peak in Figure 3a, and adjusted the gate function's duration to 4.0 fs for improved

time resolution. A zero frequency peak reaches its maximum at 12 fs in the FROG spectrogram and then decays, marking the wave packet's passage through the conical intersection at this time.

## CONCLUSIONS

So far, we have demonstrated a technique that uses a magnetic field to manipulate nonlinear spectroscopy and track molecular photochemical reactions undergoing on a femtosecond conical intersection passage.

We simulated the tr-XMCD signal to investigate the photo dissociation dynamics of pyrrole. Initiated by photo excitation of the pump pulse, the wave packet propagates on the excited state and shows the elongation of the N–H bond. It then transfers to the ground state by passing through a conical intersection. A distinct strong peak in the spectrum marks the passage of a wave packet through the CoIn generated by ground-excited electronic state coherence in the diabatic basis. In contrast to the transient-absorption spectrum whose electronic coherence peak is too weak to observe, the coherence signal strength in tr-XMCD is comparable with the population peak, making it a clear signature of a conical intersection.

Combining a magnetic field with a nonlinear spectroscopic signal provides a clear signature of conical intersection in tr-XMCD: 1) It alters the symmetry of the electric dipole response function to match the symmetry of CoIn generated electronic coherence, resulting tr-XMCD induced by the coherence, and excluding the electronic coherence created by the pump. 2) The anisotropic magnetic field response makes the coherence signal for a perpendicular magnetic field configuration particularly strong. This anisotropy originates from the molecular transition magnetic dipole, which couples the applied magnetic field to the response function. The interplay of these two effects amplifies the electronic coherence signal, making conical intersections readily observable in tr-XMCD.

In the tr-XMCD simulation, we used 1 T of a magnetic field. Since the tr-XMCD signal scales linearly with the magnetic field as depicted in eqs 10 and 12, a superconducting magnet providing 45 T magnetic field can significantly enhance the signal.

In summary, tr-XMCD is an effective technique for observing ultrafast molecular dynamics involving conical intersections. The magnetic field adds an extra control parameter in nonlinear spectroscopy, allowing for a more detailed study of photochemical reactions. We anticipate that advancements in X-ray light sources and strong magnetic fields will significantly enhance the accuracy and sensitivity of tr-XMCD, leading to more precise observations and more detailed understanding of molecular events. 73–78

## METHODS

To describe a molecular system in the presence of uniform magnetic field interacting with light pulses, we introduce a time-dependent Hamiltonian  $H(t)=H_0+V(t)$ , where  $V(t)=-\mu\cdot\mathbf{E}(t)$  is the light matter interaction between the molecule and light pulse  $(\mathbf{E}(t))$  truncated at electric dipole interaction. The time-independent Hamiltonian  $H_0$  consists of a nuclear kinetic energy term and a nonrelativistic electronic Hamiltonian that includes the interaction with a static magnetic field  $(\mathbf{B})$ .

$$H_0 = \sum_{\alpha} \frac{\mathbf{P}_{\alpha}^2}{2M_{\alpha}} + H_{0,\text{el}}(\mathbf{B})$$
 (6)

Here,  $\mathbf{P}_{\alpha} = -i\nabla_{\alpha}$  is momentum of nucleus  $\alpha$  and  $M_{\alpha}$  is its mass. Given that nuclear motion is slow compared to electronic motion, we exclude the vector potential in the nuclear momentum operator.

The many-body electronic Hamiltonian in the presence of the magnetic field is

$$H_{0,el} = \sum_{i} h_{i} - \sum_{i} \sum_{\alpha} \frac{Z_{\alpha}}{|\mathbf{r}_{i} - \mathbf{R}_{\alpha}|} + \sum_{i} \sum_{j>i} \frac{1}{|\mathbf{r}_{i} - \mathbf{r}_{j}|} + \sum_{\alpha < \beta} \frac{Z_{\alpha}Z_{\beta}}{|\mathbf{R}_{\alpha} - \mathbf{R}_{\beta}|}$$

$$(7)$$

where i's denote electrons and  $Z_{\alpha}$ 's are nuclear charges.  ${\bf r}$  and  ${\bf R}$  are electronic and nuclear coordinates, respectively.

The magnetic field enters the Hamiltonian through the minimal-coupling in the one-electron Pauli Hamiltonian.

$$h_i = \frac{1}{2} [\boldsymbol{\sigma}_i \cdot (\mathbf{p}_i + \mathbf{A}_i)]^2$$

$$= \frac{1}{2} \mathbf{p}_i^2 + \frac{1}{2} (\boldsymbol{\sigma}_i + \mathbf{r}_i \times \mathbf{p}_i) \cdot \mathbf{B} + \frac{1}{8} (\mathbf{B} \times \mathbf{r}_i)^2$$
(8)

where we used the relationship  $\mathbf{A}_i = \frac{1}{2}\mathbf{B} \times \mathbf{r}_i$  and  $\boldsymbol{\sigma}_i$  is the Pauli matrix for the electron spin. The second and third terms represent the Zeeman effect and the diamagnetic contribution, respectively. In singlet electronic states, the spin Zeeman effect  $(\boldsymbol{\sigma}_i \cdot \mathbf{B})$  is zero and only the orbital Zeeman effect,  $(\mathbf{r}_i \times \mathbf{p}_i) \cdot \mathbf{B}$ , where the magnetic field couples with the molecular angular momentum operator, contributes to the MCD signal.

The nonadiabatic molecular dynamics initiated by the pump is described by the total wave function  $\Psi(\{\mathbf{r}_i\}, \{\mathbf{R}_\alpha\}, \mathbf{B}, t)$ , governed by the time-dependent Schrödinger equation,  $i\frac{\mathrm{d}}{\mathrm{d}t}\Psi(t) = H\Psi(t)$ . Time-dependent part V(t) contains the interaction with the pump pulse that triggers the dynamics. The total wave function can be expressed using the Born–Huang expansion

$$\Psi(\{\mathbf{r}_i\}, \{\mathbf{R}_\alpha\}, \mathbf{B}, t) = \sum_{I} \Phi_I(\{\mathbf{r}_i\}, \{\mathbf{R}_\alpha\}, \mathbf{B}) \chi_I(\{\mathbf{R}_\alpha\}, t)$$
(9)

where the total wave function is projected onto the diabatic electronic basis  $\Phi_I$ . The expansion coefficient  $\chi_I$  is the nuclear wave packet of the electronic state I, describing the status of the nuclear motion. The diabatic electronic wave functions  $\Phi_I$  are constructed by unitary transformation from adiabatic electronic wave functions, which are eigenfunctions of the magnetic field contained electronic Hamiltonian (eq. 7). To initiate the dynamics, we apply the Franck–Condon approximation by placing the ground state wave packet on the excited state potential energy surface at T=0 to simulate the vertical excitation by the pump pulse. For a more accurate simulation one can include the pump pulse nonperturbatively, i.e., solve the time-dependent Schrödinger equation with explicit pump pulse in V(t).

As the wave packet evolves, the Gaussian probe pulse is applied with a variable time delay, T relative to the pump. We simulate the tr-XMCD signal with a perturbative treatment of probe pulse by evaluating the electric dipole—electric dipoles response, which integrates the nuclear wave packet, Gaussian envelope of the probe pulse, and the magnetically perturbed transition electric dipoles over space and time (eq 3).

**Electronic Structure Calculations.** The adiabatic electronic states are variationally optimized for the electronic Hamiltonian which includes the magnetic field (eq 7. We have employed a complete active space self-consistent field (CASSCF)<sup>92,93</sup> in the presence of finite magnetic field with gauge including atomic orbital (GIAO)<sup>94–97</sup> to compute the eigen states of electronic Hamiltonian eq 7 in the presence of a uniform magnetic field, including the ground state, as well as valence and core excited states. The magnetic field is variationally included in the calculation, <sup>94–101</sup> where the electronic

Hamiltonian with the magnetic field (eq 7) is used as reference Hamiltonian for this self-consistent field calculation to obtain a variational wave function in the magnetic field. The valence and the core excited states are computed at the CASSCF and CASCI level in the Chronus Quantum software package <sup>87</sup> respectively.

We include the  $\sigma$  bonding and antibonding orbitals of N–H ( $\sigma_{\rm N-H}$  and  $\sigma_{\rm N-H}^*$ ), 3  $\pi$ -bonding and 2  $\pi$ -anti bonding orbitals in the active space of CASSCF and performed state-averaged CASSCF(8,7) for the ground state  $\tilde{X}$  and excited state  $\tilde{A}$ ,  $\tilde{B}$ . For the core excited state, we used the optimized molecular orbital from CASSCF and included an additional nitrogen 1s orbital in active space to perform a CASCI(10,8) calculation. Computational details and the molecular orbitals in the active space are displayed in Supporting Information section S2. The magnetically perturbed transition electric dipole between valence and core excited states in an adiabatic basis are calculated from the variational wave functions in the magnetic field. The diabatic transition dipoles in eq 2 and 3 are obtained through the adiabatic to diabatic transformation introduced in ref 91. The core excited states are not affected by this transformation due to the absence of nonadiabatic coupling.

**Nonadiabatic Dynamics.** The photodissociation of pyrrole is simulated by wave packet dynamics of a model Hamiltonian with two nuclear degrees of freedom, the stretching (r) and the out-of-plane bending  $(\gamma)$  of the hydrogen atom (shown in Figure 1a), and two electronic states,  $\tilde{X}$  and  $\tilde{B}$ . The magnetic field is assumed sufficiently weak such that the potential energy change induced by magnetic field is negligible. The diabatic state potential energy surface fitted in refs 84 and 91 is thus used in the dynamics simulation.

The vibrational eigenstates for the electronic ground state are calculated by the discrete variable representation (DVR). This wave packet with vibrational quantum number (1,0) is placed on  $\tilde{B}$  potential energy surface as the initial wave packet to mimic the photolysis of the pump pulse,  $^{102}$  where the first and second index are for the r and  $\gamma$  coordinates, respectively.

The wave packets on  $\tilde{X}$  and  $\tilde{B}$  are calculated on a two-dimensional grid and propagated with the split-operator method. Their time evolution is solved according to the time dependent Schrödinger equation for the vibronic model,  $i\partial_t \chi_I(\mathbf{q}, t) = K\chi_I(\mathbf{q}, t) + \sum_J V_{IJ}(\mathbf{q}) \chi_J(\mathbf{q}, t)$ . K is the nuclear kinetic energy operator and V is the potential energy operator in diabatic representation. I, J are the electronic state index. The simulation details are explained in ref 82.

**Decomposition of the Electric Dipole Response.** The electric dipole response eq 2 that implicitly contains the magnetic field perturbation can be decomposed by orders of the magnetic field

$$S_{\text{XMCD},k}(T) = -i \sum_{I,J \in \text{valence}} \int d\mathbf{q} \left( \mathbf{D}_{IJ}(\mathbf{q}) \cdot \boldsymbol{\epsilon}_k \right) \rho_{JI}(\mathbf{q}, T)$$
$$= S^{(0)} + S^{(1)} \cdot \mathbf{B} + \dots$$
(10)

where  $D_{IJ}(q) = \sum_{C \in \text{core}} f_C \mu_{CI}(q) \times \mu_{C}^*(q), f_C = 2\pi\sigma^2 E_0^2 \, \mathrm{e}^{-\sigma^2(\omega_C - \omega_c)^2},$  and  $\rho_{JI}(q,T) = \chi_I(q,T) \, \chi_J^*(q,T)$ . The nonperturbative treatment of magnetic field in the simulation contains all orders of magnetic field contribution. We demonstrate that first order is the leading contribution, and the tr-XMCD signal scales linearly with magnetic field. Zeroth order is

$$S^{(0)} = \sum_{I,J \in \text{valence}, I \neq J} \int d\mathbf{q} \ (\mathbf{D}_{IJ}^{(0)}(\mathbf{q}) \cdot \boldsymbol{\epsilon}_k) \frac{-i}{2} (\rho_{JI}(\mathbf{q}) - \rho_{IJ}(\mathbf{q}))$$
(11)

where  $\mathbf{D}_{IJ}^{(0)}(\mathbf{q}) = \Sigma_{C \in \text{core}} f_C \boldsymbol{\mu}_{\tilde{C}I}^{\alpha}(\mathbf{q}) \times \boldsymbol{\mu}_{\tilde{C}I}^{\alpha}(\mathbf{q})$ . Zeroth order contribution vanishes after rotational average (see eq 4.2.48 in ref 28). For oriented molecules, the zeroth order signal is only contributed by electronic coherence where  $I \neq J$  since the transition vector product becomes zero for I = J. For pyrrole molecule, zeroth order contribution vanishes due to spatial symmetry.

The first order is

$$S_k^{(1)} = \sum_{I,J \in \text{valence}} \int d\mathbf{q} \ (\mathbf{D}_{IJ;k}^{(1)}(\mathbf{q}) \cdot \boldsymbol{\epsilon}_k) \frac{1}{2} (\rho_{JI}(\mathbf{q}) + \rho_{IJ}(\mathbf{q}))$$
(12)

where  $\mathbf{D}_{IJ;k}^{(1)}(\mathbf{q}) = \sum_{C \in \text{core}} f_C(\boldsymbol{\mu}_{CI;k}(\mathbf{q}) \times \boldsymbol{\mu}_{\mathring{C}\mathring{J}}^{\circ\circ}(\mathbf{q}) + \boldsymbol{\mu}_{CJ;k}(\mathbf{q}) \times \boldsymbol{\mu}_{\mathring{C}\mathring{I}}^{\circ\circ}(\mathbf{q}))$ , and  $\boldsymbol{\mu}_{CI;k}(\mathbf{q}) = -i \frac{\partial}{\partial B_k} \boldsymbol{\mu}_{CI}$  is the first order magnetic perturbation of transition electric dipole.

## ASSOCIATED CONTENT

## **Data Availability Statement**

All study data are included in the article and/or Supporting Information.

## Supporting Information

The Supporting Information is available free of charge at https://pubs.acs.org/doi/10.1021/jacs.4c03033.

Detailed derivation of working equations, computational details, spectra decomposition, detailed group theory analysis, perturbation analysis (PDF)

## AUTHOR INFORMATION

## **Corresponding Authors**

Shaul Mukamel — Department of Chemistry, University of California, Irvine, California 92697, United states; Department of Physics and Astronomy, University of California, Irvine, California 92697, United States; orcid.org/0000-0002-6015-3135; Email: smukamel@uci.edu

Xiaosong Li — Department of Chemistry, University of Washington, Seattle, Washington 98195, United States; orcid.org/0000-0001-7341-6240; Email: xsli@uw.edu

Shichao Sun — Department of Chemistry, University of California, Irvine, California 92697, United states; Department of Physics and Astronomy, University of California, Irvine, California 92697, United States; orcid.org/0000-0002-7680-3972; Email: shichas2@uci.edu

## **Authors**

Bing Gu — Department of Chemistry and Department of Physics, Westlake University, Hangzhou, Zhejiang 310030, China; orcid.org/0000-0002-5787-3334

Hang Hu – Department of Chemistry, University of Washington, Seattle, Washington 98195, United States Lixin Lu – Department of Chemistry, University of Washington, Seattle, Washington, 98195, United States

Washington, Seattle, Washington 98195, United States; orcid.org/0000-0003-3203-4822

Diandong Tang — Department of Chemistry, University of Washington, Seattle, Washington 98195, United States; orcid.org/0000-0003-2276-4901

Vladimir Y. Chernyak — Department of Chemistry, Wayne State University, Detroit, Michigan 48202, United States; Department of Mathematics, Wayne State University, Detroit, Michigan 48202, United States

Complete contact information is available at: https://pubs.acs.org/10.1021/jacs.4c03033

#### Notes

The authors declare no competing financial interest.

## ACKNOWLEDGMENTS

The support of the National Science Foundation through Grant No. CHE-2246379 to SM and CHE-2154346 to X.L. is gratefully acknowledged. S.S. and B.G. were supported by the U.S. Department of Energy, Office of Science, Office of Basic Energy Sciences under Award DE-FG02-04ER15571. V.Y.C. and S.M. gratefully acknowledge the support of the U.S. Department of Energy (DOE), Office of Science, Basic Energy Sciences Award DE-SC0022134.

#### REFERENCES

- (1) Domcke, W.; Yarkony, D. R. Role of Conical Intersections in Molecular Spectroscopy and Photoinduced Chemical Dynamics. *Annu. Rev. Phys. Chem.* **2012**, *63*, 325–352.
- (2) Worth, G. A.; Cederbaum, L. S. BEYOND BORN-OPPENHEIMER: Molecular Dynamics Through a Conical Intersection. *Annu. Rev. Phys. Chem.* **2004**, *55*, 127–158.
- (3) Yarkony, D. R. Diabolical conical intersections. *Rev. Mod. Phys.* **1996**, *68*, 985–1013.
- (4) Garraway, B. M.; Suominen, K.-A. Wave packet dynamics in molecules. *Contemp. Phys.* **2002**, *43*, 97–114.
- (5) Rafiq, S.; Scholes, G. D. From fundamental theories to quantum coherences in electron transfer. *J. Am. Chem. Soc.* **2018**, *141*, 708–722.
- (6) Schuurman, M. S.; Stolow, A. Dynamics at Conical Intersections. *Annu. Rev. Phys. Chem.* **2018**, *69*, 427–450.
- (7) Bircher, M. P.; Liberatore, E.; Browning, N. J.; Brickel, S.; Hofmann, C.; Patoz, A.; Unke, O. T.; Zimmermann, T.; Chergui, M.; Hamm, P.; et al. Nonadiabatic effects in electronic and nuclear dynamics. *Struct. Dyn.* **2017**, *4*, 061510.
- (8) Martínez, T. J. Ab initio molecular dynamics around a conical intersection: Li(2p) + H2. Chem. Phys. Lett. 1997, 272, 139–147.
- (9) Coe, J. D.; Martínez, T. Competitive Decay at Two- and Three-State Conical Intersections in Excited-State Intramolecular Proton Transfer. *J. Am. Chem. Soc.* **2005**, *127*, 4560–4561.
- (10) Toniolo, A.; Olsen, S.; Manohar, L.; Martínez, T. J. Conical intersection dynamics in solution: The chromophore of Green Fluorescent Protein. *Faraday Discuss.* **2004**, *127*, 149–163.
- (11) Matsika, S. Three-State Conical Intersections in Nucleic Acid Bases. J. Phys. Chem. A 2005, 109, 7538–7545.
- (12) Coe, J. D.; Martínez, T. Ab Initio Molecular Dynamics of Excited-State Intramolecular Proton Transfer around a Three-State Conical Intersection in Malonaldehyde. *J. Phys. Chem. A* **2006**, *110*, 618–630.
- (13) Virshup, A. M.; Chen, J.; Martínez, T. Nonlinear dimensionality reduction for nonadiabatic dynamics: The influence of conical intersection topography on population transfer rates. *J. Chem. Phys.* **2012**, *137*, 22A519.
- (14) Zewail, A. H. Femtochemistry: Atomic-scale dynamics of the chemical bond using ultrafast lasers (Nobel Lecture). *Angew. Chem., Int. Ed.* **2000**, *39*, 2586–2631.
- (15) Zewail, A. H. Femtochemistry: Atomic-Scale Dynamics of the Chemical Bond. *J. Phys. Chem. A* **2000**, *104*, 5660–5694.
- (16) Mukamel, S. Principles of Nonlinear Optical Spectroscopy; Oxford University Press, 1995.
- (17) Neville, S. P.; Chergui, M.; Stolow, A.; Schuurman, M. S. Ultrafast X-Ray Spectroscopy of Conical Intersections. *Phys. Rev. Lett.* **2018**, *120*, 243001.
- (18) Glownia, J. M.; Natan, A.; Cryan, J. P.; Hartsock, R.; Kozina, M.; Minitti, M. P.; Nelson, S.; Robinson, J.; Sato, T.; van Driel, T.; Welch, G.; Weninger, C.; Zhu, D.; Bucksbaum, P. H. Self-Referenced Coherent Diffraction X-Ray Movie of Ångstrom- and Femtosecond-Scale Atomic Motion. *Phys. Rev. Lett.* **2016**, *117*, 153003.
- (19) Bennett, K.; Kowalewski, M.; Rouxel, J. R.; Mukamel, S. Monitoring molecular nonadiabatic dynamics with femtosecond X-ray diffraction. *Proc. Natl. Acad. Sci. U.S.A.* **2018**, *115*, 6538–6547.
- (20) Yong, H.; Keefer, D.; Mukamel, S. Imaging purely nuclear quantum dynamics in molecules by combined x-ray and electron diffraction. *J. Am. Chem. Soc.* **2022**, *144*, 7796–7804.
- (21) von Conta, A.; Tehlar, A.; Schletter, A.; Arasaki, Y.; Takatsuka, K.; Wörner, H. J. Conical-intersection dynamics and ground-state

- chemistry probed by extreme-ultraviolet time-resolved photoelectron spectroscopy. *Nat. Commun.* **2018**, *9*, 3162.
- (22) Cavaletto, S. M.; Keefer, D.; Mukamel, S. Electronic Coherences in Nonadiabatic Molecular Photophysics Revealed by Time-resolved Photoelectron Spectroscopy. *Proc. Natl. Acad. Sci. U.S.A.* 2022, 119, e2121383119.
- (23) Polli, D.; Altoè, P.; Weingart, O.; Spillane, K. M.; Manzoni, C.; Brida, D.; Tomasello, G.; Orlandi, G.; Kukura, P.; Mathies, R. A.; Garavelli, M.; Cerullo, G. Conical intersection dynamics of the primary photoisomerization event in vision. *Nature* **2010**, *467*, 440–443.
- (24) Kowalewski, M.; Bennett, K.; Dorfman, K. E.; Mukamel, S. Catching Conical Intersections in the Act: Monitoring Transient Electronic Coherences by Attosecond Stimulated X-Ray Raman Signals. *Phys. Rev. Lett.* **2015**, *115*, 193003.
- (25) Keefer, D.; Schnappinger, T.; de Vivie-Riedle, R.; Mukamel, S. Visualizing conical intersection passages via vibronic coherence maps generated by stimulated ultrafast X-ray Raman signals. *Proc. Natl. Acad. Sci. U.S.A.* **2020**, *117*, 24069–24075.
- (26) Cho, D.; Rouxel, J. R.; Mukamel, S. Stimulated X-ray resonant Raman spectroscopy of conical intersections in thiophenol. *J. Phys. Chem. Lett.* **2020**, *11*, 4292–4297.
- (27) Keefer, D.; Freixas, V. M.; Song, H.; Tretiak, S.; Fernandez-Alberti, S.; Mukamel, S. Monitoring molecular vibronic coherences in a bichromophoric molecule by ultrafast X-ray spectroscopy. *Chem. Sci.* **2021**, *12*, 5286–5294.
- (28) Barron, L. D. Molecular Light Scattering and Optical Activity; Cambridge University Press, 2009.
- (29) Piepho, S. B.; Schatz, P. N. Group Theory in Spectroscopy: with Applications to Magnetic Circular Dichroism; Wiley-Interscience, 1983; Vol. 1.
- (30) Mason, W. R. A Practical Guide to Magnetic Circular Dichroism Spectroscopy; John Wiley & Sons, Inc.: Hoboken, NJ, 2006.
- (31) Hassan, M. T.; Luu, T. T.; Moulet, A.; Raskazovskaya, O.; Zhokhov, P.; Garg, M.; Karpowicz, N.; Zheltikov, A.; Pervak, V.; Krausz, F.; Goulielmakis, E. Optical Attosecond Pulses and Tracking the Nonlinear Response of Bound Electrons. *Nature* **2016**, *530*, 66–70
- (32) Ferré, A.; et al. A table-top ultrashort light source in the extreme ultraviolet for circular dichroism experiments. *Nat. Photonics* **2015**, *9*, 93–98.
- (33) Kfir, O.; Grychtol, P.; Turgut, E.; Knut, R.; Zusin, D.; Popmintchev, D.; Popmintchev, T.; Nembach, H.; Shaw, J. M.; Fleischer, A.; Kapteyn, H.; Murnane, M.; Cohen, O. Generation of bright phase-matched circularly-polarized extreme ultraviolet high harmonics. *Nat. Photonics* **2015**, *9*, 99–105.
- (34) Paul, P.-M.; Toma, E. S.; Breger, P.; Mullot, G.; Augé, F.; Balcou, P.; Muller, H. G.; Agostini, P. Observation of a train of attosecond pulses from high harmonic generation. *Science* **2001**, *292*, 1689–1692.
- (35) Drescher, M.; Hentschel, M.; Kienberger, R.; Tempea, G.; Spielmann, C.; Reider, G. A.; Corkum, P. B.; Krausz, F. X-ray pulses approaching the attosecond frontier. *Science* **2001**, *291*, 1923–1927.
- (36) Baltuška, A.; Udem, T.; Uiberacker, M.; Hentschel, M.; Goulielmakis, E.; Gohle, C.; Holzwarth, R.; Yakovlev, V. S.; Scrinzi, A.; Hänsch, T. W.; Krausz, F. Attosecond control of electronic processes by intense light fields. *Nature* **2003**, *421*, 611–615.
- (37) Hentschel, M.; Kienberger, R.; Spielmann, C.; Reider, G. A.; Milosevic, N.; Brabec, T.; Corkum, P.; Heinzmann, U.; Drescher, M.; Krausz, F. Attosecond metrology. *Nature* **2001**, *414*, 509–513.
- (38) López-Martens, R.; Varjú, K.; Johnsson, P.; Mauritsson, J.; Mairesse, Y.; Salières, P.; Gaarde, M. B.; Schafer, K. J.; Persson, A.; Svanberg, S.; Wahlström, C.-G.; L'Huillier, A. Amplitude and Phase Control of Attosecond Light Pulses. *Phys. Rev. Lett.* **2005**, *94*, 033001.
- (39) Hartmann, N.; et al. Attosecond time-energy structure of X-ray free-electron laser pulses. *Nat. Photonics* **2018**, *12*, 215–220.
- (40) Wang, J.; Bulanov, S. V.; Chen, M.; Lei, B.; Zhang, Y.; Zagidullin, R.; Zorina, V.; Yu, W.; Leng, Y.; Li, R.; Zepf, M.;

- Rykovanov, S. G. Relativistic slingshot: A source for single circularly polarized attosecond x-ray pulses. *Phys. Rev. E* **2020**, *102*, 061201.
- (41) Schütz, G.; Wagner, W.; Wilhelm, W.; Kienle, P.; Zeller, R.; Frahm, R.; Materlik, G. Absorption of circularly polarized x rays in iron. *Phys. Rev. Lett.* **1987**, *58*, 737.
- (42) Stewart, B.; Peacock, R. D.; Alagna, L.; Prosperi, T.; Turchini, S.; Goulon, J.; Rogalev, A.; Goulon-Ginet, C. Circular dichroism at the edge: Large X-ray natural CD in the 1s→ 3d pre-edge feature of 2 [Co (en) 3Cl3]· NaCl· 6H2O. *J. Am. Chem. Soc.* 1999, 121, 10233–10234.
- (43) Rogalev, A.; Goulon, J.; Wilhelm, F. X-ray detected optical activity. *Comptes Rendus Physique* **2008**, *9*, 642–656. (Synchrotron X-rays and condensed matter).
- (44) Goldbeck, R. A.; Dawes, T. D.; Einarsdottir, O.; Woodruff, W. H.; Kliger, D. S. Time-resolved magnetic circular dichroism spectroscopy of photolyzed carbonmonoxy cytochrome c oxidase (cytochrome aa3). *Biophys. J.* **1991**, *60*, 125–134.
- (45) Kliger, D.; Lewis, J. Recent advances in time resolved circular dichroism spectroscopy. *Res. Chem. Intermediat.* **1987**, *8*, 367–398.
- (46) O'Connor, D.; Goldbeck, R.; Hazzard, J.; Kliger, D.; Cusanovich, M. Time-resolved absorption and magnetic circular dichroism spectroscopy of cytochrome c3 from Desulfovibrio. *Biophys. J.* 1993, 65, 1718–1726.
- (47) Goldbeck, R. A.; Dawes, T. D.; Milder, S. J.; Lewis, J. W.; Kliger, D. S. Measurement of magnetic circular dichroism (MCD) on a nanosecond timescale. *Chem. Phys. Lett.* **1989**, *156*, 545–549.
- (48) Goldbeck, R. A.; Kim-Shapiro, D. B.; Kliger, D. S. Fast Natural and Magnetic Circular Dichroism Spectroscopy. *Annu. Rev. Phys. Chem.* **1997**, 48, 453–479.
- (49) Chen, C. T.; Sette, F.; Ma, Y.; Modesti, S. Soft-x-ray magnetic circular dichroism at the  $L_{2,3}$  edges of nickel. *Phys. Rev. B* **1990**, 42, 7262–7265.
- (50) Fan, T.; Grychtol, P.; Knut, R.; Hernández-García, C.; Hickstein, D. D.; Zusin, D.; Gentry, C.; Dollar, F. J.; Mancuso, C. A.; Hogle, C. W.; et al. Bright circularly polarized soft X-ray high harmonics for X-ray magnetic circular dichroism. *Proc. Natl. Acad. Sci. U.S.A.* **2015**, *112*, 14206–14211.
- (51) Wu, R.; Wang, D.; Freeman, A. First Principles Investigation of the Validity and Range of Applicability of the X-ray Magnetic Circular Dichroism Sum Rule. *Phys. Rev. Lett.* **1993**, *71*, 3581.
- (52) Chen, C.; Idzerda, Y.; Lin, H.-J.; Smith, N.; Meigs, G.; Chaban, E.; Ho, G.; Pellegrin, E.; Sette, F. Experimental Confirmation of the X-ray Magnetic Circular Dichroism Sum Rules for Iron and Cobalt. *Phys. Rev. Lett.* **1995**, *75*, 152.
- (53) Stöhr, J. Exploring the microscopic origin of magnetic anisotropies with X-ray magnetic circular dichroism (XMCD) spectroscopy. J. Magn. Magn. Mater. 1999, 200, 470–497.
- (54) Funk, T.; Deb, A.; George, S. J.; Wang, H.; Cramer, S. P. X-ray magnetic circular dichroism—a high energy probe of magnetic properties. *Coordin. Chem. Rev.* **2005**, 249, 3–30.
- (55) van der Laan, G. Applications of soft x-ray magnetic dichroism. *J. Phys.: Conf. Ser.* **2013**, 430, 012127.
- (56) van der Laan, G.; Figueroa, A. I. X-ray magnetic circular dichroism—A versatile tool to study magnetism. *Coordin. Chem. Rev.* **2014**, 277, 95–129.
- (57) Hennes, M.; Rösner, B.; Chardonnet, V.; Chiuzbaian, G. S.; Delaunay, R.; Döring, F.; Guzenko, V. A.; Hehn, M.; Jarrier, R.; Kleibert, A.; Jal, E.; et al. Time-resolved XUV absorption spectroscopy and magnetic circular dichroism at the Ni M 2, 3-edges. *Appl. Sci.* **2021**, *11*, 325.
- (58) Zamudio-Bayer, V.; Hirsch, K.; Langenberg, A.; Kossick, M.; Ławicki, A.; Terasaki, A.; v. Issendorff, B.; Lau, J. T. Direct observation of high-spin states in manganese dimer and trimer cations by x-ray magnetic circular dichroism spectroscopy in an ion trap. *J. Chem. Phys.* **2015**, *142*, 234301.
- (59) Zamudio-Bayer, V.; Hirsch, K.; Langenberg, A.; Niemeyer, M.; Vogel, M.; Ławicki, A.; Terasaki, A.; Lau, J. T.; Von Issendorff, B. Maximum Spin Polarization in Chromium Dimer Cations as

- Demonstrated by X-ray Magnetic Circular Dichroism Spectroscopy. *Angew. Chem., Int. Ed.* **2015**, *54*, 4498–4501.
- (60) Kowalska, J. K.; Henthorn, J. T.; Van Stappen, C.; Trncik, C.; Einsle, O.; Keavney, D.; DeBeer, S. X-ray Magnetic Circular Dichroism Spectroscopy Applied to Nitrogenase and Related Models: Experimental Evidence for a Spin-Coupled Molybdenum (III) Center. *Angew. Chem., Int. Ed.* **2019**, *58*, 9373–9377.
- (61) Akin, S. T.; Zamudio-Bayer, V.; Duanmu, K.; Leistner, G.; Hirsch, K.; Bülow, C.; Ławicki, A.; Terasaki, A.; Von Issendorff, B.; Truhlar, D. G.; Lau, J. T.; Duncan, M. A. Size-dependent ligand quenching of ferromagnetism in Co3 (benzene) n+ clusters studied with X-ray magnetic circular dichroism spectroscopy. *J. Phys. Chem. Lett.* 2016, 7, 4568–4575.
- (62) Marcham, M. K.; Shelford, L. R.; Cavill, S. A.; Keatley, P. S.; Yu, W.; Shafer, P.; Neudert, A.; Childress, J. R.; Katine, J. A.; Arenholz, E.; Telling, N. D.; van der Laan, G.; Hicken, R. J. Phaseresolved x-ray ferromagnetic resonance measurements of spin pumping in spin valve structures. *Phys. Rev. B* **2013**, *87*, 180403.
- (63) Goulon, J.; Rogalev, A.; Goujon, G.; Wilhelm, F.; Youssef, J. B.; Gros, C.; Barbe, J.-M.; Guilard, R. X-ray detected magnetic resonance: a unique probe of the precession dynamics of orbital magnetization components. *Int. J. Mol. Sci.* **2011**, *12*, 8797–8835.
- (64) Boero, G.; Rusponi, S.; Bencok, P.; Popovic, R.; Brune, H.; Gambardella, P. X-ray ferromagnetic resonance spectroscopy. *Appl. Phys. Lett.* **2005**, *87*, 152503.
- (65) Takubo, K.; Yamamoto, K.; Hirata, Y.; Yokoyama, Y.; Kubota, Y.; Yamamoto, S.; Yamamoto, S.; Matsuda, I.; Shin, S.; Seki, T.; et al. Capturing ultrafast magnetic dynamics by time-resolved soft x-ray magnetic circular dichroism. *Appl. Phys. Lett.* **2017**, *110*, 162401.
- (66) Boeglin, C.; Beaurepaire, E.; Halté, V.; López-Flores, V.; Stamm, C.; Pontius, N.; Dürr, H.; Bigot, J.-Y. Distinguishing the ultrafast dynamics of spin and orbital moments in solids. *Nature* **2010**, 465, 458–461.
- (67) Bergeard, N.; López-Flores, V.; Halte, V.; Hehn, M.; Stamm, C.; Pontius, N.; Beaurepaire, E.; Boeglin, C. Ultrafast Angular Momentum Transfer in Multisublattice Ferrimagnets. *Nat. Commun.* **2014**, *5*, 3466.
- (68) Thole, B.; Van der Laan, G. Sum rules for magnetic dichroism in rare earth 4f photoemission. *Phys. Rev. Lett.* **1993**, *70*, 2499.
- (69) Thole, B.; Carra, P.; Sette, F.; van der Laan, G. X-ray circular dichroism as a probe of orbital magnetization. *Phys. Rev. Lett.* **1992**, 68, 1943.
- (70) Carra, P.; Thole, B.; Altarelli, M.; Wang, X. X-ray circular dichroism and local magnetic fields. *Phys. Rev. Lett.* **1993**, *70*, 694.
- (71) Altarelli, M. Orbital-magnetization sum rule for x-ray circular dichroism: A simple proof. *Phys. Rev. B* **1993**, *47*, 597.
- (72) Van der Laan, G. Sum rules and fundamental spectra of magnetic x-ray dichroism in crystal field symmetry. *J. Phys. Soc. Jpn.* **1994**, *63*, 2393–2400.
- (73) Schneider-Muntau, H.; Brandt, B.; Brunel, L.; Cross, T.; Edison, A.; Marshall, A.; Reyes, A. The National High Magnetic Field Laboratory. *Physica B* **2004**, *346*–*347*, 643–648. (Proceedings of the Seventh International Symposium on Research in High Magnetic Fields)
- (74) Jaime, M.; Lacerda, A.; Takano, Y.; Boebinger, G. S. The National High Magnetic Field Laboratory. *J. Phys.: Conf. Ser.* **2006**, *51*, *643*.
- (75) Wang, Q.; et al. Progress of ultra-high-field superconducting magnets in China. Supercond. Sci. Technol. 2022, 35, 023001.
- (76) Chen, W.; Huang, P.; Tan, Y.; Li, J.; Pan, Y.; Chen, Z.; Chen, Z.; Zhu, J.; Fang, Z.; Kuang, G. Construction of cryostat components for the CHMFL hybrid magnet superconducting outsert. *IEEE Trans. Appl. Supercond.* **2016**, 26, 1–4.
- (77) Maiuri, M.; Oviedo, M. B.; Dean, J. C.; Bishop, M.; Kudisch, B.; Toa, Z. S. D.; Wong, B. M.; McGill, S. A.; Scholes, G. D. High Magnetic Field Detunes Vibronic Resonances in Photosynthetic Light Harvesting. *J. Phys. Chem. Lett.* **2018**, *9*, 5548–5554.
- (78) Kudisch, B.; Maiuri, M.; Moretti, L.; Oviedo, M. B.; Wang, L.; Oblinsky, D. G.; Prud'homme, R. K.; Wong, B. M.; McGill, S. A.;

- Scholes, G. D. Ring currents modulate optoelectronic properties of aromatic chromophores at 25 T. *Proc. Natl. Acad. Sci. U.S.A.* **2020**, 117, 11289–11298.
- (79) Ahmad, S.; Alam, O.; Naim, M. J.; Shaquiquzzaman, M.; Alam, M. M.; Iqbal, M. Pyrrole: An insight into recent pharmacological advances with structure activity relationship. *Eur. J. Med. Chem.* **2018**, 157, 527–561.
- (80) Dervan, P. B.; Edelson, B. S. Recognition of the DNA minor groove by pyrrole-imidazole polyamides. *Curr. Opin. Struct. Biol.* **2003**, *13*, 284–299.
- (81) Best, T. P.; Edelson, B. S.; Nickols, N. G.; Dervan, P. B. Nuclear localization of pyrrole—imidazole polyamide—fluorescein conjugates in cell culture. *Proc. Natl. Acad. Sci. U.S.A.* **2003**, *100*, 12063—12068.
- (82) Gu, B.; Sun, S.; Chen, F.; Mukamel, S. Photoelectron spectroscopy with entangled photons; enhanced spectrotemporal resolution. *Proc. Natl. Acad. Sci. U.S.A.* **2023**, *120*, e2300541120.
- (83) Wu, G.; Neville, S. P.; Schalk, O.; Sekikawa, T.; Ashfold, M. N. R.; Worth, G. A.; Stolow, A. Excited state non-adiabatic dynamics of pyrrole: A time-resolved photoelectron spectroscopy and quantum dynamics study. *J. Chem. Phys.* **2015**, *142*, 074302.
- (84) Vallet, V.; Lan, Z.; Mahapatra, S.; Sobolewski, A. L.; Domcke, W. Time-dependent quantum wave-packet description of the 1  $\pi\sigma^*$  photochemistry of pyrrole. *Faraday Discuss.* **2004**, *127*, 283–293.
- (85) Xie, C.; Malbon, C. L.; Yarkony, D. R.; Xie, D.; Guo, H. Signatures of a conical intersection in adiabatic dissociation on the ground electronic state. *J. Am. Chem. Soc.* **2018**, *140*, 1986–1989.
- (86) Campbell, J.; Papp, T. Widths of the Atomic K-N7 Levels. At. Data Nucl. Data Tables 2001, 77, 1-56.
- (87) Williams-Young, D. B.; Petrone, A.; Sun, S.; Stetina, T. F.; Lestrange, P.; Hoyer, C. E.; Nascimento, D. R.; Koulias, L.; Wildman, A.; Kasper, J.; et al. The Chronus Quantum (ChronusQ) Software Package. Wiley Interdiscip. Rev.: Comput. Mol. Sci. 2020, 10, e1436.
- (88) Cotton, F. A. Chemical Applications of Group Theory; John Wiley & Sons, 2003.
- (89) Stephens, P. Magnetic circular dichroism. Annu. Rev. Phys. Chem. 1974, 25, 201–232.
- (90) Hahn, S.; Kim, K.; Kim, K.; Hu, X.; Painter, T.; Dixon, I.; Kim, S.; Bhattarai, K. R.; Noguchi, S.; Jaroszynski, J.; Larbalestier, D. C. 45.5-T direct-current magnetic field generated with a high-temperature superconducting magnet. *Nature* **2019**, *570*, 496–499.
- (91) Vallet, V.; Lan, Z.; Mahapatra, S.; Sobolewski, A. L.; Domcke, W. Photochemistry of pyrrole: Time-dependent quantum wave-packet description of the dynamics at the  $\pi$  1  $\sigma^*$ -S 0 conical intersections. *J. Chem. Phys.* **2005**, *123*, 144307.
- (92) Jenkins, A. J.; Liu, H.; Kasper, J. M.; Frisch, M. J.; Li, X. Variational Relativistic Complete Active Space Self-Consistent Field Method. *J. Chem. Theory Comput.* **2019**, *15*, 2974–2982.
- (93) Jenkins, A. J.; Hu, H.; Lu, L.; Frisch, M. J.; Li, X. Two-Component Multireference Restricted Active Space Configuration Interaction for the Computation of L-Edge X-ray Absorption Spectra. *J. Chem. Theory Comput.* **2022**, *18*, 141–150.
- (94) Sun, S.; Williams-Young, D.; Li, X. An Ab Initio Linear Response Method for Computing Magnetic Circular Dichroism Spectra with Nonperturbative Treatment of Magnetic Field. *J. Chem. Theory Comput.* **2019**, *15*, 3162–3169.
- (95) Sun, S.; Williams-Young, D.; Stetina, T. F.; Li, X. Generalized Hartree-Fock with Non-perturbative Treatment of Strong Magnetic Field: Application to Molecular Spin Phase Transition. *J. Chem. Theory Comput.* **2019**, *15*, 348–356.
- (96) Sun, S.; Beck, R.; Williams-Young, D. B.; Li, X. Simulating Magnetic Circular Dichroism Spectra with Real-Time Time-Dependent Density Functional Theory in Gauge Including Atomic Orbitals. *J. Chem. Theory Comput.* **2019**, *15*, 6824–6831.
- (97) Sun, S.; Li, X. Relativistic Effects in Magnetic Circular Dichroism: Restricted Magnetic Balance and Temperature Dependence. J. Chem. Theory Comput. 2020, 16, 4533–4542.
- (98) Tellgren, E. I.; Soncini, A.; Helgaker, T. Nonperturbative ab initio Calculations in Strong Magnetic Fields Using London Orbitals. *J. Chem. Phys.* **2008**, *129*, 154114.

- (99) Lange, K. K.; Tellgren, E. I.; Hoffmann, M.; Helgaker, T. A Paramagnetic Bonding Mechanism for Diatomics in Strong Magnetic Fields. *Science* **2012**, *337*, 327–331.
- (100) Tellgren, E. I.; Teale, A. M.; Furness, J. W.; Lange, K.; Ekström, U.; Helgaker, T. Non-Perturbative Calculation of Molecular Magnetic Properties within Current-Density Functional Theory. *J. Chem. Phys.* **2014**, *140*, 034101.
- (101) Sen, S.; Tellgren, E. I. Non-Perturbative Calculation of Orbital and Spin Effects in Molecules Subject to Non-Uniform Magnetic Fields. *J. Chem. Phys.* **2018**, *148*, 184112.
- (102) Colbert, D. T.; Miller, W. H. A novel discrete variable representation for quantum mechanical reactive scattering via the Smatrix Kohn method. *J. Chem. Phys.* **1992**, *96*, 1982–1991.
- (103) Kosloff, R. Time-dependent quantum-mechanical methods for molecular dynamics. *J. Phys. Chem.* **1988**, *92*, 2087–2100.

# **Supporting Information:**

# Direct Probe of Conical Intersection Photochemistry by Time-Resolved X-ray Magnetic Circular Dichroism

Shichao Sun,\* $,\dagger,\parallel$  Bing Gu, $^\ddagger$  Hang Hu, $^\P$  Lixin Lu, $^\P$  Diandong Tang, $^\P$  Vladimir Y. Chernyak, $^{\S,\perp}$  Xiaosong Li, $^*,^\P$  and Shaul Mukamel $^*,^\dagger,\#$ 

†Department of Chemistry, University of California, Irvine, CA 92697, USA

‡Department of Chemistry & Department of Physics, Westlake University, Hangzhou,

Zhejiang 310030, China

¶Department of Chemistry, University of Washington, Seattle, WA 98195, USA

§Department of Chemistry, Wayne State University, 5101 Cass Ave, Detroit, Michigan

48202, USA

|| Department of Physics and Astronomy, University of California, Irvine, CA 92697CA 92697, USA

⊥Department of Mathematics, Wayne State University, 656 W. Kirby, Detroit, Michigan 48202, USA

#Department of Physics and Astronomy, University of California, Irvine, CA 92697, USA

E-mail: shichas2@uci.edu; xsli@uw.edu; smukamel@uci.edu

# Contents

S1 Derivation of the Expressions for the Time-resolved Signal		
2 Derivation of the Frequency- and Time-Resolved Magnetic Circular	r Dichro-	
ism Signal	S-7	
3 CASSCF Calculation	S-12	
4 Population and Coherence Contribution in XMCD	S-13	
5 Coupling with the Magnetic Field	S-13	
S5.A No Magnetic Field	S-16	
S5.B The Signal Coupled with the Magnetic Field	S-17	
S5.C The Transition Magnetic Dipoles	S-18	
S5.D Magnetic Induced Current Density	S-18	
References	S-19	

# S1 Derivation of the Expressions for the Time-resolved Signal

In this section we present a derivation for the CD signals. We start with the time-resolved signal. We will use a time-integrated (at the detector) signal with no frequency resolution, since the ultrashort nature of the probe pulse provides with the desired time resolution, so that the time-integrated signal is considered as a function of the pulse time delay.

The time-integrated signal, associated with a spectroscopic measurement device can be generally represented in a from

$$S = \int_{\mathbb{R}} dt \langle \mathcal{E}_L^-(\mathbf{r}_D, t) \cdot \mathcal{E}_R^+(\mathbf{r}_D, t) \rangle, \tag{S1}$$

where  $\mathcal{E}_{L,R}^{\pm}$  are the Liouville space negative/positive frequency quantum (operator or path-integral) electric field variables, and the expectation value is taken in Liouville space for the system with the sources, responsible for the pump and probe laser field generation.

Since for the pump-probe setting, the field generated by the probe-induced polarization in the sample and the probe counterpart propagate in the same direction, the pump-probe signal can be viewed as a self-heterodyne, i.e., in the first non-vanishing order, it is generated by mixing the probe field with the polarization-generated counterpart. Upon expanding to first order in the probe field, the following expression for the excited state absorption that dominates the signal and is obtained by choosing the proper Liouville space pathways adopts a form

$$S_{EA} = \int_{\mathbb{R}} dt \int_{-\infty}^{t} dt_{1} \mathcal{D}(t - t_{1}; \boldsymbol{r}_{D}, \boldsymbol{r}) (\operatorname{Tr}(-i\hat{\boldsymbol{\mu}}\rho_{L}^{(1)}(t_{1})) \cdot \boldsymbol{E}^{+*}(\boldsymbol{r}_{D}, t))$$

$$\times \int_{\mathbb{R}} dt \int_{-\infty}^{t} dt_{1} \mathcal{D}(t - t_{1}; \boldsymbol{r}_{D}, \boldsymbol{r}) (\operatorname{Tr}(i\rho_{R}^{(1)}(t_{1})\hat{\boldsymbol{\mu}}) \cdot \boldsymbol{E}^{+}(\boldsymbol{r}_{D}, t)), \tag{S2}$$

where  $E^+(r_D, t)$  is the positive-frequency component of the probe field at the detector,  $\mathcal{D}$  is the retarded Green function of the Maxwell equations, and

$$\rho_L^{(1)}(t_1) = \int_{-\infty}^{t_1} dt_2 e^{-i(t_1 - t_2)H} (-i\hat{\boldsymbol{\mu}}\rho(t_2)) e^{i(t_1 - t_2)H} \cdot \boldsymbol{E}^+(\boldsymbol{r}, t_2), 
\rho_R^{(1)}(t_1) = \int_{-\infty}^{t_1} dt_2 e^{-i(t_1 - t_2)H} (i\rho(t_2)\hat{\boldsymbol{\mu}}) e^{i(t_1 - t_2)H} \cdot \boldsymbol{E}^{+*}(\boldsymbol{r}, t_2)$$
(S3)

are two contributions to the first-order in the probe field density matrix of the molecule, where  $\rho(t_2)$  is the molecular density matrix photo-excited by the pump field. In deriving Eqs. (S2) and (S3) we made use of the fact that in vacuum  $\langle \mathcal{E}_L^- \mathcal{E}_R^+ \rangle = 0$ , while the choice of the left and right actions of  $\mu$  in the first and second expression in Eq. (S3), respectively, is associated with adopting the rotating-wave approximation for the excited-state absorption contribution to the pump-probe signal.

Applying the Huegens-Fresnel-Kirchhoff principle to express the probe field at the detec-

tor in terms of its value at the molecule, making use of the fact that up to a fudge factor the field at the molecule is given by a simple time shift of the field at the molecule (which boils down to effectively considering the detector to be placed right at the molecule), making use of the pure-state nature of the density matrix  $\rho(t_1) = |\Psi(t_1)\rangle\langle\Psi(t_1)|$ , and substituting Eq. (S3) into Eq. (S2) we obtain

$$S_{EA} = - \int_{\mathbb{R}} dt \int_{-\infty}^{t} dt_{1} E_{j}(t_{1}) E_{k}^{*}(t) \operatorname{Tr}(\hat{\mu}_{k} e^{-i(t-t_{1})H} \hat{\mu}_{j}) |\Psi(t_{1})\rangle \langle \Psi(t_{1})| e^{i(t-t_{1})H})$$

$$- \int_{\mathbb{R}} dt \int_{-\infty}^{t} dt_{1} E_{j}^{*}(t_{1}) E_{k}(t) \operatorname{Tr}(e^{-i(t-t_{1})H}) |\Psi(t_{1})\rangle \langle \Psi(t_{1})| \hat{\mu}_{j} e^{i(t-t_{1})H} \hat{\mu}_{k}). \quad (S4)$$

We further represent the molecular state as

$$\Psi(\boldsymbol{q}, t_1) = \sum_{A} \chi_{\alpha}(\boldsymbol{q}, t_1) \Phi_A(\boldsymbol{q}), \tag{S5}$$

with  $(\Phi_A(q) | A \in \{\tilde{X}, \tilde{B}\})$  being the molecular configuration dependent basis set in the space of the relevant dissociating electronic states, and make use of the fact that the X-ray probe pulse is short compared to the time scale of vibrational motions, as well as the inverse energy ranges of the adiabatic surfaces in the relevant range of molecular configurations and the energy gap between the dissociating states. The latter circumstance allows to introduce the molecular configuration independent transition frequencies  $\omega_C$  between the core states, labeled by C, and the dissociating counterparts, as well as approximating the molecular evolution at the time interval  $[t_1, t]$  by purely electron term dynamics, resulting in

$$\operatorname{Tr}(\hat{\mu}_{k}e^{-i(t-t_{1})H}\hat{\mu}_{j})|\Psi(t_{1})\rangle\langle\Psi(t_{1}|e^{i(t-t_{1})H}) = \sum_{C}e^{-i\omega_{C}(t-t_{1})}\sum_{AD}\int d\boldsymbol{q}\mu_{k}^{DC}(\boldsymbol{q})\mu_{CA}^{j}((\boldsymbol{q})\rho_{AD}(\boldsymbol{q}),(S6)$$

where

$$\rho_{AD}(\mathbf{q}) = \chi_A^*(\mathbf{q})\chi_D(\mathbf{q}) \tag{S7}$$

is the molecular configration dependent electronic density matrix, and

$$\mu_{CA}(\mathbf{q}) = \langle \Phi_C(\mathbf{q}) | \hat{\boldsymbol{\mu}} | \Phi_A(\mathbf{q}) \rangle \tag{S8}$$

are the transition dipoles between the dissociating and core states. The transition dipoles and electronic state energies are in the presence of the magnetic field, and we neglected the effects of the magnetic field on the wavepacket dynamics.

For a Gaussian circularly polarized pulse

$$\mathbf{E}^{+}(t) = E_0 e^{-i\omega_c (t-T)} e^{-(t-T)^2/(2\sigma^2)} \boldsymbol{\epsilon}, \tag{S9}$$

we substitute Eq. (S6) into Eq. (S4), consider the difference between the left- and rightpolarized probe signals  $S_{EA}$ , and making use of  $[\epsilon, \epsilon^*] = \mp i n$  for the left and right circular polarization, with n being the probe propagation direction, we obtain, after some straightforward linear algebra

$$S_{CD} = -i \sum_{AD} \int d\mathbf{q} (\mathbf{D}_{AD}(\mathbf{q}) \cdot \mathbf{n}) \rho_{DA}(\mathbf{q}, T), \quad \tilde{\mathbf{D}}_{AD}(\mathbf{q}) = \sum_{C} f_{C}[\boldsymbol{\mu}_{CA}(\mathbf{q}), \boldsymbol{\mu}_{CD}^{*}(\mathbf{q})], \quad (S10)$$

where the weight factors have a form

$$f_C = \int_{\mathbb{R}} dt_1 \int_{\mathbb{R}} dt_2 e^{-t_1^2/(2\sigma^2) - t_2^2/(2\sigma^2)} e^{-i(\omega_C - \omega_c)(t_1 - t_2)}$$
(S11)

Note that the contributions of the two terms in Eq. (S4) to the expression for  $f_C$  correspond to the integration regions  $t_1 \le t_2$  and  $t_2 \le t_1$ . In the sum of these contributions, the time integration goes over the complete real line, resulting in an explicit expression

$$f_C = 2\pi\sigma^2 |E_0^2| e^{-\sigma^2(\omega_C - \omega_c)^2},$$
 (S12)

allowing for a natural interpretation: the signal is given by the weighted sum of contribu-

tions, associated with the transitions between the dissociating and core states, which are in resonance with the probe pulse within its spectral width.

Up to first order in the magnetic field, the signal adopts a form

$$S = S^{(0)} + (\mathbf{S}^{(1)} \cdot \mathbf{B}), \tag{S13}$$

with

$$S^{(0)} = \sum_{AB} \int d\mathbf{q} (\mathbf{D}_{AD}^{(0)}(\mathbf{q}) \cdot \mathbf{n}) \frac{-i}{2} (\rho_{DA}(\mathbf{q}, T) - \rho_{AD}(\mathbf{q}, T)),$$

$$\mathbf{D}_{AD}^{(0)}(\mathbf{q}) = \sum_{C} f_{C}[\boldsymbol{\mu}_{\mathring{C}\mathring{A}}(\mathbf{q}), \boldsymbol{\mu}_{\mathring{C}\mathring{D}}(\mathbf{q})], \quad \mathbf{D}_{AD}^{(0)}(\mathbf{q}) = -\mathbf{D}_{DA}^{(0)}(\mathbf{q}), \tag{S14}$$

where we have used the real nature of the matrix elements  $\mu_{\mathring{C}\mathring{A}}$  of the real operator  $\hat{\mu}$  between real electronic states, and

$$S_{j}^{(1)} = \sum_{AD} \int d\mathbf{q} (\mathbf{D}_{AD;j}^{(1)}(\mathbf{q}) \cdot \mathbf{n}) \frac{1}{2} (\rho_{DA}(\mathbf{q}) + \rho_{AD}(\mathbf{q})),$$

$$\mathbf{D}_{AD;j}^{(1)}(\mathbf{q}) = \sum_{C} f_{C}([\boldsymbol{\mu}_{CA;j}(\mathbf{q}), \boldsymbol{\mu}_{\mathring{C}\mathring{D}}(\mathbf{q})] + [\boldsymbol{\mu}_{CD;j}(\mathbf{q}), \boldsymbol{\mu}_{\mathring{C}\mathring{A}}(\mathbf{q})]),$$

$$\boldsymbol{\mu}_{CA;j}(\mathbf{q}) = -i \frac{\partial}{\partial B_{j}} \langle \Phi_{C}(\mathbf{q}) | \hat{\boldsymbol{\mu}} | \Phi_{A}(\mathbf{q}) \rangle |_{\boldsymbol{B}=0}, \quad \mathbf{D}_{AD;j}^{(1)}(\mathbf{q}) = \mathbf{D}_{DA;j}^{(1)}(\mathbf{q})$$
(S15)

and we have used the real nature of the matrix elements  $\mu_{CA;j}(x)$ .

To understand the invariant nature of the signals with respect to a basis set choice in the space of the electronic dissociation states, we note that the Pauli matrices form a basis set in the space of traceless Hermitian  $2 \times 2$  matrices, allowing a decomposition of any Hermitian matrix

$$A_{AD} = A_0 \sigma_{0,AD} + \sum_{s=1}^{3} A_s \sigma_{s,AD}, \quad \bar{A}_2 = iA_2,$$
 (S16)

where  $\sigma_0$  is the identity matrix. Decomposing  $i\boldsymbol{D}$ ,  $\boldsymbol{D}_j^{(1)}$  and  $\rho$  in the Pauli matrices, we

recast the signals [Eqs. (S14) and (S15)] in a form

$$S^{(0)} = \int d\mathbf{x} (\bar{\mathbf{D}}_2(\mathbf{x}) \cdot \mathbf{n}) \bar{\rho}_2(\mathbf{x}), \tag{S17}$$

$$S_j^{(1)} = \int d\mathbf{x} (\mathbf{D}_{0,j}(\mathbf{x}) \cdot \mathbf{n}) \rho_0(\mathbf{x}) + \sum_{a=1,3} \int d\mathbf{x} (\mathbf{D}_{a,j}(\mathbf{x}) \cdot \mathbf{n}) \rho_a(\mathbf{x}), \quad (S18)$$

and the components of the density matrix in Eqs. (S17) and (S18) that have an explicit form

$$\rho_0 = \frac{1}{2}(\rho_{11} + \rho_{22}), \quad \rho_1 = \frac{1}{2}(\rho_{12} + \rho_{21}) \quad \bar{\rho}_2 = -\frac{i}{2}(\rho_{12} - \rho_{21}), \quad \rho_3 = \frac{1}{2}(\rho_{11} - \rho_{22}), \quad (S19)$$

represent the total populaiton of the two levells, the real part of the coherence, the imaginary part of the coherence, and the difference of the populations.

It is worth mentioning that under an orthogonal transformation of a real basis set (that preserve orthonormality and real nature of it), represented by a rotation  $S(\theta)$ , the Pauli matrices  $\sigma_0$  and  $\sigma_2$  stay unchanged, while the pair  $(\sigma_1, \sigma_3)$  experiences a rotation  $S(2\theta)$ . This implies that the components  $\rho_0$ ,  $\mathbf{D}_{0,j}$ ,  $\bar{\rho}_2$ , and  $\bar{\mathbf{D}}_2$  do not depend on the basis choice, i.e., they are invariantly defined. The other components are not invariant with respect to the basis set rotations, however, the pairs  $(\rho_1, \rho_3)$  and  $(\mathbf{D}_{1,j}, \mathbf{D}_{3,j})$  experience the same rotation  $S(2\theta)$  [inherited from the rotation  $S(2\theta)$  of the corresponding Pauli matrices], and, therefore, the second term in the r.h.s. of the second expression in Eq. (S19) is the basis set choice independent, as it should be by a simple reason that it represents a contribution to the signal, the latter knowing nothing about our basis set choices.

# S2 Derivation of the Frequency- and Time-Resolved Magnetic Circular Dichroism Signal

The dynamics initiated by the pump pulse is simulated by the non-adiabatic dynamics. Here we derive the tr-MCD signal induced by the probe pulse.

Define a Gaussian-enveloped wave with an electric field amplitude  $E_0$ , central frequency  $\omega_c$  and duration  $\sigma$ ,  $\mathbf{E}(t) = E_0 e^{-\frac{(t-T)^2}{2\sigma^2}} i(\boldsymbol{\epsilon} e^{-i\omega_c(t-T)} - \boldsymbol{\epsilon}^* e^{i\omega_c(t-T)}) = \mathbf{E}_-(t) + \mathbf{E}_+(t)$ . The dipole interaction between the molecule and probe light is described by the interaction Hamiltonian, which, with rotating wave approximation, is

$$H_{\text{int}} = -iE_0 e^{-\frac{(t-T)^2}{2\sigma^2}} \left( \boldsymbol{\mu}^+ \cdot \boldsymbol{\epsilon} e^{-i\omega_c(t-T)} - \boldsymbol{\mu}^- \cdot \boldsymbol{\epsilon}^* e^{i\omega_c(t-T)} \right)$$
 (S20)

where  $\mu^+$  and  $\mu^-$  are excitation and deexcitation operators.

The electric field  $\boldsymbol{E}(t)$  can be expanded by frequency components  $\boldsymbol{E}(t) = E_0 \frac{1}{2\pi} \int_{-\infty}^{\infty} d\omega i \left[ -\boldsymbol{\epsilon}^* e^{i\omega t} \tilde{W}_+(\omega) + \boldsymbol{\epsilon} e^{-i\omega t} \tilde{W}_-(\omega) \right]$ , where

$$\tilde{W}_{+}(\omega) = \int_{-\infty}^{\infty} dt e^{-i\omega t} e^{-\frac{(t-T)^2}{2\sigma^2}} e^{i\omega_c(t-T)} = \sqrt{2\pi}\sigma \left[e^{-i\omega T} e^{-\frac{\sigma^2}{2}(\omega-\omega_c)^2}\right]$$
(S21)

$$\tilde{W}_{-}(\omega) = \int_{-\infty}^{\infty} dt e^{i\omega t} e^{-\frac{(t-T)^2}{2\sigma^2}} e^{-i\omega_c(t-T)} = \sqrt{2\pi}\sigma \left[e^{i\omega T} e^{-\frac{\sigma^2}{2}(\omega-\omega_c)^2}\right]$$
(S22)

In quantized form,

$$\boldsymbol{E}(t) = E_0 \frac{1}{2\pi} \int_{-\infty}^{\infty} d\omega i \left[ -a_{\omega}^{\dagger} \boldsymbol{\epsilon}^* e^{i\omega t} \tilde{W}_{+}(\omega) + a_{\omega} \boldsymbol{\epsilon} e^{-i\omega t} \tilde{W}_{-}(\omega) \right]$$
 (S23)

$$H_{int} = -\frac{E_0}{2\pi} \int_{-\infty}^{\infty} d\omega i \left[ -a_{\omega}^{\dagger} \boldsymbol{\mu}^{-} \cdot \boldsymbol{\epsilon}^{*} e^{i\omega t} \tilde{W}_{+}(\omega) + a_{\omega} \boldsymbol{\mu}^{+} \cdot \boldsymbol{\epsilon} e^{-i\omega t} \tilde{W}_{-}(\omega) \right]$$
 (S24)

The heterodyne signal measures the change of photon number at certain frequency  $\omega$ ,

$$\int dt \langle \dot{N}_{\omega} \rangle \tag{S25}$$

By operator algebra, we have

$$\dot{N}_{\omega} = -\frac{iE_{0}}{2\pi\hbar} \int_{-\infty}^{\infty} d\omega i \left[ a_{\omega}^{\dagger} \boldsymbol{\mu}^{-} \cdot \boldsymbol{\epsilon}^{*} e^{i\omega t} \tilde{W}^{+}(\omega) + a_{\omega} \boldsymbol{\mu}^{+} \cdot \boldsymbol{\epsilon} e^{-i\omega t} \tilde{W}^{-}(\omega) \right] 
= -\frac{E_{0}}{\pi\hbar} \int_{-\infty}^{\infty} d\omega \Im \left[ \boldsymbol{\mu}^{-} \cdot (-i) \boldsymbol{\epsilon}^{*} a_{\omega}^{\dagger} W_{+}(\omega) e^{i\omega t} \right].$$
(S26)

The signal at photon frequency  $\omega$  is

$$S(\omega) = -\frac{1}{\pi \hbar} E_0 \Im[\tilde{W}_+(\omega) \int dt \, (-i) a_\omega^{\dagger} \langle \boldsymbol{\mu}^- \cdot \boldsymbol{\epsilon}^* \rangle e^{i\omega t}]$$
 (S27)

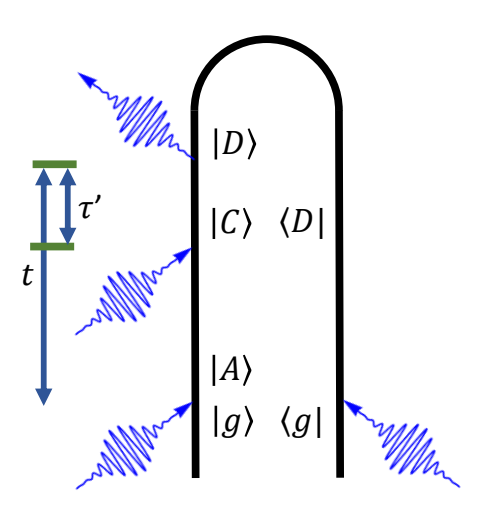


**Figure S1.** Ladder diagram of X-ray TRXCD. We only consider the excited state absorption contribution.

To first order, from Fig. S1, with rotating wave approximation, we have first order expression

$$S^{(1)}(\omega, T) = -\frac{1}{\pi \hbar} E_0 \Im \left[ \tilde{W}_+(\omega)(-i) \int_{-\infty}^{\infty} dt \, e^{i\omega t} \int_{t}^{-\infty} d\tau' \left( -\frac{i}{\hbar} \left\langle \boldsymbol{\mu}^- \cdot \boldsymbol{\epsilon}^* \, \boldsymbol{\mu}^+ \cdot \boldsymbol{E}_-(t - \tau') \right\rangle \right) \right]$$
(S28)

change from Heisenberg picture to Schrödinger picture,

$$S^{(1)}(\omega, T) = -\frac{1}{\pi h} E_0 \Im[\tilde{W}_+(\omega)(-i) \int_{-\infty}^{\infty} dt \, e^{i\omega t} \int_{t}^{-\infty} d\tau' \left( -\frac{i}{h} \right) \left( \mu^- \cdot \epsilon^* U(\tau') \mu^+ \cdot E_-(t - \tau') \right) \right]$$
(S29)

where  $U(\tau')$  is the time evolution of core excited states. The lifetime of core excited states are short. We thus make frozen nuclei approximation, i.e., for the core excited states, the nuclear motion is ignored and we only consider the time evolution of electronic wave function. Expand with electronic states, the bracket expression can be expressed as

$$S^{(1)}(\omega, T) = -\frac{1}{\pi \hbar} E_0 \, \Im[\tilde{W}_+(\omega)(-i) \int_{-\infty}^{\infty} dt \, e^{i(\omega - \omega_c)t} \int_{t}^{-\infty} d\tau' \left( -\frac{i}{\hbar} \right) e^{i\omega_c(\tau' + T)} \mathcal{E}(t - \tau' - T)$$

$$\int d\boldsymbol{q} \, \chi_D^*(\boldsymbol{q}, t) \boldsymbol{\mu}_{DC} \cdot \boldsymbol{\epsilon}^* e^{-i(\omega_C - i\Gamma)\tau'} \boldsymbol{\mu}_{CA} \cdot \boldsymbol{\epsilon} \chi_A(\boldsymbol{q}, t - \tau')]$$
(S30)

where  $\mathcal{E}(t-T) = E_0 e^{-\frac{(t-T)^2}{2\sigma^2}}$ . Circular dichroism is the absorption of left circulary polarized light minus the right. By definition,

$$S^{(1)}(\omega, T) = -\frac{1}{\pi \hbar} E_0 \mathcal{I}[\tilde{W}_+(\omega)(-i) \int_{-\infty}^{\infty} dt \, e^{i(\omega - \omega_c)t} \int_{t}^{-\infty} d\tau' \left( -\frac{i}{\hbar} \right) e^{i\omega_c(\tau' + T)} \mathcal{E}(t - \tau' - T)$$

$$\int d\boldsymbol{q} \, \chi_D^*(\boldsymbol{q}, t) e^{-i(\omega_C - i\Gamma)\tau'} (\boldsymbol{\mu}_{DC} \cdot \boldsymbol{\epsilon}_-^* \boldsymbol{\mu}_{CA} \cdot \boldsymbol{\epsilon}_- - \boldsymbol{\mu}_{DC} \cdot \boldsymbol{\epsilon}_+^* \boldsymbol{\mu}_{CA} \cdot \boldsymbol{\epsilon}_+) \chi_A(\boldsymbol{q}, t - \tau')]$$
(S31)

The circular dichroism is defined as the difference of absorption of left and right circularly polarized light,  $S_{CD} = S_- - S_+$ . Define the polarization unit vector of circularly polarized wave as  $\boldsymbol{\epsilon}_{\pm}(\gamma) = \frac{1}{\sqrt{2}}(\boldsymbol{\epsilon}_{\alpha} \pm i\boldsymbol{\epsilon}_{\beta})$ , where  $\gamma$  is the propagation direction of the wave,  $\alpha$ ,  $\beta$  and  $\gamma$  are perpendicular to each other and follow right hand rule. Specially, a wave propagating in z direction has circular polarization  $\boldsymbol{\epsilon}_{\pm}(z) = \frac{1}{\sqrt{2}}(\boldsymbol{\epsilon}_x \pm i\boldsymbol{\epsilon}_y)$ . Here the unit vector of propagation

direction vector is  $\boldsymbol{\epsilon}_{\kappa}$ , we have relation

$$p \cdot \epsilon_{-}^{*} q \cdot \epsilon_{-} - p \cdot \epsilon_{+}^{*} q \cdot \epsilon_{+} = -ip \times q \cdot \epsilon_{\kappa}$$

where  $\mathbf{p}$  and  $\mathbf{q}$  are arbitrary vectors. So the signal becomes

$$S^{\text{XMCD}}(\omega, T) = \frac{1}{\pi \hbar} E_0 \Im \left[ \tilde{W}_+(\omega) \int_{-\infty}^{\infty} dt \, e^{i(\omega - \omega_c)t} \int_{t}^{-\infty} d\tau' \left( -\frac{i}{\hbar} \right) e^{i\omega_c(\tau' + T)} \mathcal{E}(t - \tau' - T) \right]$$

$$\int d\mathbf{q} \, \chi_D^*(\mathbf{q}, t) e^{-i(\omega_C - i\Gamma)\tau'} (\boldsymbol{\mu}_{DC} \times \boldsymbol{\mu}_{CA} \cdot \boldsymbol{\epsilon}_{\kappa}) \chi_A(\mathbf{q}, t - \tau') \right]$$
(S32)

Adjust the equation a bit, we have

$$S^{\text{XMCD}}(\omega, T) = \frac{1}{\pi \hbar} E_0 \Im \left[ \sqrt{2\pi} \sigma \left( e^{-i(\omega - \omega_c)T} e^{-\frac{\sigma^2}{2}(\omega - \omega_c)^2} \right) \int_{-\infty}^{\infty} dt \, e^{i(\omega - \omega_c)t} \left( -\frac{i}{\hbar} \right) \right]$$

$$\int_{t}^{-\infty} d\tau' \mathcal{E}(t - \tau' - T) \int d\mathbf{q} \, \chi_D^*(\mathbf{q}, t) e^{i\omega_c \tau'} e^{-i(\omega_C - i\Gamma)\tau'} (\boldsymbol{\mu}_{DC} \times \boldsymbol{\mu}_{CA} \cdot \boldsymbol{\epsilon}_{\kappa}) \chi_A(\mathbf{q}, t - \tau')$$
(S33)

To ensure numerical stability, we do substitution of variable for  $\tau'$ 

$$\int_{t}^{-\infty} d\tau' \mathcal{E}(t - \tau' - T) \int d\boldsymbol{q} \, \chi_{D}^{*}(\boldsymbol{q}, t) e^{i\omega_{c}\tau'} e^{-i(\omega_{C} - i\Gamma)\tau'} (\boldsymbol{\mu}_{DC} \times \boldsymbol{\mu}_{CA} \cdot \boldsymbol{\epsilon}_{\kappa}) \chi_{A}(\boldsymbol{q}, t - \tau')$$

$$\stackrel{\delta=t-\tau'}{=} - \int_{-\infty}^{t} d\delta \, \mathcal{E}(\delta - T) \int d\boldsymbol{q} \, \chi_{D}^{*}(\boldsymbol{q}, t) e^{-i(\omega_{C} - \omega_{c})(t - \delta)} (\boldsymbol{\mu}_{DC} \times \boldsymbol{\mu}_{CA} \cdot \boldsymbol{\epsilon}_{\kappa}) \chi_{A}(\boldsymbol{q}, \delta) e^{-\Gamma(t - \delta)} \quad (S34)$$

So the work equation becomes

$$S^{\text{XMCD}}(\omega, T)) = \frac{1}{\pi \hbar^{2}} E_{0} \Re\left[\sqrt{2\pi}\sigma \left(e^{-i(\omega-\omega_{c})T}e^{-\frac{\sigma^{2}}{2}(\omega-\omega_{c})^{2}}\right) \int_{-\infty}^{\infty} dt \, e^{i(\omega-\omega_{C})t} \right]$$

$$\int_{-\infty}^{t} d\delta \, \mathcal{E}(\delta - T) \int d\boldsymbol{q} \, \chi_{D}^{*}(\boldsymbol{q}, t) e^{i(\omega_{C} - \omega_{c})\delta} (\boldsymbol{\mu}_{DC} \times \boldsymbol{\mu}_{CA} \cdot \boldsymbol{\epsilon}_{\kappa}) \chi_{A}(\boldsymbol{q}, \delta) e^{-\Gamma(t-\delta)} \right]$$
(S35)

## S3 CASSCF Calculation

The geometry of the pyrrole molecule is optimized with B3LYP density functional with 6-311++g(d,p) basis function S1-S4 in Gaussian 16 software package. S5 The electronic eigen states are computed with complete active space self consistent field (CASSCF) in a development version of Chronus Quantum software package. S6 7 active orbitals are chosen as N-H  $\sigma$  bond and  $\sigma^*$  anti-bond, 5  $\pi$  orbitals of pyrrole, and a Rydberg anti-bonding orbital, see Fig. S2. 8 electrons are in the active space. State average over ground state  $({}^{1}A_{1})$ , first  $(^{1}A_{2})$  and second excited state  $(^{1}B_{1})$  is performed. Non-relativistic Pauli Hamiltonian in Eq. (2) and Eq. (3) in the main text is used for the self consistent field calculation. The variational wave function is solved with finite magnetic field. We use gauge including atomic orbital (GIAO) as the basis function to define gauge origin at nucleus and enforce gauge origin invariance. Augmented correlation-consistent polarized valence double-zeta (aug-ccpVDZ) basis is used in both CASSCF calculations. One additional diffuse s function and one additional set of p functions were added to the nitrogen atom. Two additional diffuse s and two additional sets of diffuse p functions were added to all the hydrogen atom. Their exponents were derived in an even-tempered manner from the most diffuse s and p functions already present in the aug-cc-pVDZ basis by dividing the exponents successively by a factor of 3.0.57 For core excited states, we add nitrogen 1s orbital in the previous active space and perform complete active space configuration interaction (CASCI) with the set of molecular orbitals obtained in the previous CASSCF calculation.

For the potential energy surface of core excited states, we scan the  $r_{\text{N-H}}$  =0.91, 1.41, 1.81, 2.21, 2.61, 4.14 Å and out of plane bending angle -50°, -10°, 0°, 10°, 50°, and interpolate the potential energy surface for Jacobi coordinate  $r, \gamma$ . The transition dipoles are computed with  $r_{\text{N-H}}$  =0.91 Å and out of plane bending angle -50°, -10°, 0°, 10°, 50°. The computations are performed with magnetic field applied in x, y, z directions respectively.

# S4 Population and Coherence Contribution in XMCD

To analyze the tr-XMCD spectrum, we separately depict the population term (A = D in Eq. (S35)) and coherence term  $(A \neq D \text{ in Eq. (S35)})$  contribution. We choose diabatic electronic states as basis. The signal is invariant with respect to basis choice. Here we do this separation for explanation and analysis purpose only.

The oriented molecule tr-XMCD spectrum with magnetic field in x is separated in Fig. S3. The coherence contribution shows strong peak when the wave packet passes through conical intersection, while the population contribution is weak by comparison. From this, we conclude that the signature of conical intersection in the tr-XMCD spectrum is contributed by electronic coherence.

Tr-XMCD of oriented molecule with parallel magnetic field is displayed in Fig. S4. The electronic coherence contribution Fig. S4a is weak. As the wave packet gradually relax from excited state to ground state, the  $\tilde{X}$  electronic state population peak (Fig. S4b) gets stronger while the  $\tilde{B}$  electronic state population peak (Fig. S4b) gets weaker.

We also analyze the transient absorption spectrum. Its coherence signal (Fig. S5a) reflects the conical intersection. However, such coherence signal is too weak to observe since it is buried in the much stronger population signal (Fig. S5b).

# S5 Coupling with the Magnetic Field

In this section, we analyze the circular dichroism of the  $\tilde{X}$  –  $\tilde{B}$  coherence with irreducible representation in the  $C_{2v}$  point group. Define  $S^{CD}$  as a function of dissociation coordinate r and out of plane bending angle  $\gamma$ ,

$$S_{DA}^{\rm CD}(r,\gamma) = \boldsymbol{\mu}_{DC} \times \boldsymbol{\mu}_{CA} \cdot \boldsymbol{\epsilon}_{\kappa} \tag{S36}$$

the integration of CD signal with wavepacket can be written as

$$\int d\boldsymbol{q} \, \chi_D^*(\boldsymbol{q}, t) e^{i(\omega_C - \omega_c)\delta} (\boldsymbol{\mu}_{DC} \times \boldsymbol{\mu}_{CA} \cdot \boldsymbol{\epsilon}_{\kappa}) \chi_A(\boldsymbol{q}, \delta) ]$$

$$= \int dr \int d\gamma \, \chi_D^*(r, \gamma, t) S_{CD}(r, \gamma) \chi_A(r, \gamma, \delta)$$
(S37)

The nuclear wave packet of  $\tilde{B}(\chi_{\tilde{B}})$  is an even function of the out of plane bending motion while  $\tilde{X}(\chi_{\tilde{X}})$  is an odd function. We can derive the irrep of the nuclear wave packet  $\chi_{\tilde{X}}$  and  $\chi_{\tilde{B}}$ . The out of plane bending motion is a motion of H atom in x direction, belonging to B<sub>1</sub> irrep. For the nuclear wave packet, since the bending in y direction is frozen, the reflection with respect to xz plane character of  $\tilde{B}$  and  $\tilde{X}$  wave packet are the same. Without losing generality, we define them as even. For the reflection with respect to yz plane, wave packet  $\tilde{X}$ and  $\tilde{B}$  are odd and even respectively. Thus, the irreducible representation of  $\tilde{X}$  and  $\tilde{B}$  wave packets are  $B_1$  and  $A_1$  respectively. The irrep of the  $\tilde{X}$  –  $\tilde{B}$  coherence can also be explained from the non-adiabatic coupling.  $\chi_{\tilde{B}}$  wave packet relaxes to the ground state through the non-adiabatic coupling of CoIn and generate wave packet  $\chi_{\tilde{X}}$ . The non-adiabatic coupling of the bending coordinate is strong, while the non-adiabatic coupling of motion in y is weak and thus ignored. The derivative with respect to  $\gamma$  changes the quantum number of from 0 in  $\chi_{\tilde{B}}$  to 1 in  $\chi_{\tilde{X}}$  for bending motion, while leaving the motion in y unchanged. The product of  $\tilde{B}$  and  $\hat{X}$  is thus an even function of reflection with respect to xz plane since they have the same parity for y coordinate.  $\chi_{\tilde{B}}\chi_{\tilde{X}}$  has odd parity of reflection with respect to yz plane since  $\tilde{B}$  and  $\tilde{X}$  have opposite parity, caused by the non-adiabatic coupling. For that reason, the electronic coherence have the same irrep (and parity symmetry) as the non-adiabatic coupling.

For  $\tilde{X}$  –  $\tilde{B}$  coherence term in XMCD signal,  $S_{\tilde{X},\tilde{B}}^{\text{CD}}(r,\gamma)$  must be odd with respect to  $\gamma$  such that the integration does not vanish. Since the out of plane bending of hydrogen is in x direction, the CD signal must be odd with respect to reflection operation with  $\sigma_{yz}$  plane.

For zero magnetic field, function  $S_{\tilde{X}.\tilde{B}}^{\text{CD}}$  can be written as transition dipole product

$$S_{\tilde{X},\tilde{B}}^{\text{CD,nomag}} = \epsilon_{ijk} \langle \tilde{X} | \mu_i | C \rangle \langle C | \mu_j | \tilde{B} \rangle$$
 (S38)

where C is core excited state, k is the propagation direction of the probing wave. When the magnetic field is applied in k direction, when there is no degeneracy, the first order perturbation of wave function can be written as  $|A^{(1)}\rangle = \sum_{D\neq A} |\mathring{D}\rangle \frac{\langle \mathring{D}|m_k|\mathring{A}\rangle}{\mathring{E}_A - \mathring{E}_D}$ , where D is all possible intermediate state, "indicates electronic eigenstate in the absence of a magnetic field. The perturbed quantity  $S^{\text{CD}}$  can be expanded with a series of magnetic field. The first order contribution is

$$\frac{\langle \mathring{X}|m_{k}|\mathring{D}\rangle}{\mathring{E}_{\tilde{X}} - \mathring{E}_{D}} \langle \mathring{D}|\mu_{i}|\mathring{C}\rangle \langle \mathring{C}|\mu_{j}|\mathring{\tilde{B}}\rangle + \langle \mathring{\tilde{X}}|\mu_{i}|\mathring{C}\rangle \langle \mathring{C}|\mu_{j}|\mathring{D}\rangle \frac{\langle \mathring{D}|m_{k}|\mathring{\tilde{B}}\rangle}{\mathring{E}_{\tilde{B}} - \mathring{E}_{D}} + 
\langle \mathring{\tilde{X}}|\mu_{i}|\mathring{D}\rangle \frac{\langle \mathring{D}|m_{k}|\mathring{C}\rangle}{\mathring{E}_{C} - \mathring{E}_{D}} \langle \mathring{C}|\mu_{j}|\mathring{\tilde{B}}\rangle + \langle \mathring{\tilde{X}}|\mu_{i}|\mathring{C}\rangle \frac{\langle \mathring{C}|m_{k}|\mathring{D}\rangle}{\mathring{E}_{C} - \mathring{E}_{D}} \langle \mathring{D}|\mu_{j}|\mathring{\tilde{B}}\rangle$$
(S39)

Among the four terms in Eq. (S39) the first and second terms have larger magnitude than the third and fourth due to the larger denominator in the latter two. Since the density of states in the X-ray region is low for the molecule of interest, the energy gap  $\mathring{E}_C - \mathring{E}_D$  is large, making the contribution from the third and fourth term negligible compared with the first and second term. The contribution from the second term is greater than the first term, since the energy gap  $\mathring{E}_{\tilde{X}} - \mathring{E}_D$  larger than  $\mathring{E}_{\tilde{B}} - \mathring{E}_D$  as depicted in Tab. S3. Eq. (S39) is important for analyzing the magnetic anisotropy of tr-XMCD later. Eq. (S39) can be also given in the form of first derivative

$$S_{\tilde{X},\tilde{B}}^{\text{CD,mag}} = \epsilon_{ijk} \frac{\partial \langle \tilde{X} | \mu_i | C \rangle^k \langle C | \mu_j | \tilde{B} \rangle^k}{\partial B_k} \bigg|_{B=0} B_k$$
 (S40)

here we introduce superscript k for transition dipole to emphasize that this quantity is in the perturbation of magnetic field in k direction.

Now we show that  $S_{\tilde{X}.\tilde{B}}^{\text{CD,mag}}$  have irreducible representation  $B_1$  so that its integration with

wave packet  $\chi_{\tilde{X}}, \chi_{\tilde{B}}$  is nonzero, while the integration of  $S_{\tilde{X},\tilde{B}}^{\text{CD,nomag}}$  with wave packet is zero.

We first prove that in the absence of magnetic field, the coherence CD signal is zero.

## S5.A No Magnetic Field

In Eq. (S38), the irreducible representation of the transition dipole  $\langle \tilde{X} | \mu_i | C \rangle$  and  $\langle C | \mu_j | \tilde{B} \rangle$  can be obtained from  $\Gamma_{\tilde{X}} \otimes \Gamma_{\mu_i} \otimes \Gamma_C$  and  $\Gamma_C \otimes \Gamma_{\mu_j} \otimes \Gamma_{\tilde{B}}$  respectively.

**Table S1.** Circuar Dichroism Irreducible Representation in the Absence of Magnetic Field

Component $k$	$\Gamma_{\langle \tilde{X}   \mu_i   C \rangle} =$	$\Gamma_{\langle C \mu_j \tilde{B} angle}=$	coherence
	$\Gamma_{\tilde{X}} \otimes \Gamma_{\mu_i} \otimes \Gamma_C$	$\Gamma_C \otimes \Gamma_{\mu_j} \otimes \Gamma_{\tilde{B}}$	$S_{\text{nomag}}$
	$\langle \tilde{X}   \mu_y   C \rangle$	$\langle C \mu_z \tilde{B}\rangle$	A
	$A_1 \otimes B_2 \otimes A_1 = B_2$	$A_1 \otimes A_1 \otimes B_1 = B_1$	$A_2$
X	$\langle \tilde{X}   \mu_z   C \rangle$	$\langle C \mu_y \tilde{B}\rangle$	Λ
	$A_1 \otimes A_1 \otimes A_1 = A_1$	$A_1 \otimes B_2 \otimes B_1 = A_2$	$A_2$
	$\langle \tilde{X}   \mu_x   C \rangle$	$\langle C \mu_z \tilde{B}\rangle$	Α.
У	$A_1 \otimes B_1 \otimes A_1 = B_1$	$A_1 \otimes A_1 \otimes B_1 = B_1$	$A_1$
	$\langle \tilde{X}   \mu_z   C \rangle$	$\langle C \mu_x \tilde{B}\rangle$	Λ
	$A_1 \otimes A_1 \otimes A_1 = A_1$	$A_1 \otimes B_1 \otimes B_1 = A_1$	$A_1$
z	$\langle \tilde{X}   \mu_x   C \rangle$	$\langle C \mu_y \tilde{B}\rangle$	D
	$A_1 \otimes B_1 \otimes A_1 = B_1$	$A_1 \otimes B_2 \otimes B_1 = A_2$	$B_2$
	$\langle \tilde{X}   \mu_y   C \rangle$	$\langle C \mu_x \tilde{B}\rangle$	D
	$A_1 \otimes B_2 \otimes A_1 = B_2$	$A_1 \otimes B_1 \otimes B_1 = A_1$	$B_2$

State  $\tilde{X}$  and  $\tilde{B}$  correspond to irrep  $A_1$  and  $B_1$  respectively. The electric dipole operator  $\mu_x$ ,  $\mu_y$ ,  $\mu_z$  correspond to  $B_1$ ,  $B_2$ ,  $A_1$  respectively. So The core excited state which is from 1s (N) to  $\sigma^*$  is  $A_1$ . The irreps of  $S_{\tilde{X},\tilde{B}}^{\text{CD,nomag}}$  with probing wave propagating in x, y, z directions are summarized in Tab. S2. None of them have  $B_1$  representation. Thus, the cross term CD signal vanishes in the absence of magnetic field.

## S5.B The Signal Coupled with the Magnetic Field

We now prove that when the magnetic field is applied, the cross term MCD signal does not vanish.

The magnetic field is coupled to the molecule through magnetic dipole interaction  $(m_k, k = x, y, z)$ , the magnetic dipole operator in x, y, z direction correspond to B<sub>2</sub>, B<sub>1</sub>, A<sub>2</sub> respectively. The irrep of  $S_{\tilde{X},\tilde{B}}^{\text{CD,mag}}$  is the product of the irreps of transition dipoles and a magnetic dipole operator

$$\Gamma_{\langle \tilde{X} | \mu_i | C \rangle} \otimes \Gamma_{\langle C | \mu_i | \tilde{B} \rangle} \otimes \Gamma_{m_k}$$
 (S41)

The irreducible representation of intermediate state B does not change the signal symmetry since it appear twice in every term of Eq. (S39) and  $\Gamma_B \otimes \Gamma_B = A_1$ , which does not change the final irreducible representation.

As shown in Tab. S2, the cross term of MCD signal for magnetic field applied in x, y, z directions has  $B_1$  irreducible representation. As explained in the main text, wave packet  $\chi_{\tilde{X}}$  has  $B_1$  irrep while  $\chi_{\tilde{B}}$  is  $A_1$ . As a result, integration Eq. (S37) does not vanish and the cross term in the XMCD signal gives the signature of conical intersection.

Table S2. Magnetic Circuar Dichroism Irreducible Representation.

magnatic fold (D.)	$\Gamma_{\langle \tilde{X} \mu_i C\rangle} =$	$\Gamma_{\langle C \mu_i \tilde{B}\rangle} =$	cross term	
magnetic field $(B_k)$	$\Gamma_{\tilde{X}} \otimes \Gamma_{\mu_i} \otimes \Gamma_C$	$\Gamma_C \otimes \Gamma_{\mu_j} \otimes \Gamma_{\tilde{B}}$	MCD	
$B_x (m_x \sim B_2)$	$\langle \tilde{X}   \mu_y   C \rangle$	$\langle C \mu_z \tilde{B}\rangle$	D	
	$A_1 \otimes B_2 \otimes A_1 = B_2$	$A_1 \otimes A_1 \otimes B_1 = B_1$	$B_1$	
	$\overline{\langle \tilde{X}   \mu_z   C \rangle}$	$\langle C \mu_y \tilde{B}\rangle$	D	
	$A_1 \otimes A_1 \otimes A_1 = A_1$	$A_1 \otimes B_2 \otimes B_1 = A_2$	$B_1$	
$B_y (m_y \sim B_1)$	$\langle \tilde{X}   \mu_x   C \rangle$	$\langle C \mu_z \tilde{B}\rangle$	D	
	$A_1 \otimes B_1 \otimes A_1 = B_1$	$A_1 \otimes A_1 \otimes B_1 = B_1$	$B_1$	
	$\langle \tilde{X}   \mu_z   C \rangle$	$\langle C \mu_x \tilde{B}\rangle$	D	
	$A_1 \otimes A_1 \otimes A_1 = A_1$	$A_1 \otimes B_1 \otimes B_1 = A_1$	$B_1$	
$B_z (m_z \sim A_2)$	$\langle \tilde{X}   \mu_x   C \rangle$	$\langle C \mu_y \tilde{B}\rangle$	D	
	$A_1 \otimes B_1 \otimes A_1 = B_1$	$ig   ext{ }  ext{A}_1 \otimes  ext{B}_2 \otimes  ext{B}_1 =  ext{A}_2$	$B_1$	
	$\langle \tilde{X}   \mu_y   C \rangle$	$\langle C \mu_x \tilde{B}\rangle$	D	
	$A_1 \otimes B_2 \otimes A_1 = B_2$	$A_1 \otimes B_1 \otimes B_1 = A_1$	$B_1$	

## S5.C The Transition Magnetic Dipoles

We summarize the nonzero transition magnetic dipoles among lowest valence states at Frank-Condon geometry.

**Table S3.** State to State Transition Magnetic Dipole of Pyrrole Molecule at Frank-Condon Geometry. The transition magnetic dipoles  $\langle e_1 | \boldsymbol{m} | e_2 \rangle$  are in atomic unit  $\hbar e/m_e$ .

transition				
magnetic dipole	x component	y  component	z component	energy gap (eV)
$\langle  ilde{B}   m{m}    ilde{A}  angle$	0.6802 i	0.0	0.0	0.6274
$\langle  ilde{B}   m{m}    ilde{X}  angle$	0.0	0.3528 i	0.0	4.9279
$\langle  ilde{A}   m{m}    ilde{X}  angle$	0.0	0.0	-0.3907 i	4.3005

At this geometry, the magnitude of transition magnetic dipole between state  $\tilde{B}$  and  $\tilde{A}$  is the strongest. Additionally, the energy gap between  $\tilde{B}$  and  $\tilde{A}$  is the smallest. Since the magnetic coupling strength is proportional with transition magnetic dipole and the inverse of the state energy difference, overall, the coupling with in x direction is one order of magnitude stronger than other direction for the cross term XMCD signal.

# S5.D Magnetic Induced Current Density

As depicted in the Fig. S6, we present the current density of the electronic ground state  $(\mathbf{j}_{\tilde{X},\tilde{B}})$  and  $\tilde{B}$  excited state  $(\mathbf{j}_{\tilde{B},\tilde{B}})$ , as well as transition current density  $(\mathbf{j}_{\tilde{X},\tilde{B}})$ . In the absence of magnetic field,  $\mathbf{j}_{\tilde{X},\tilde{X}}$  and  $\mathbf{j}_{\tilde{B},\tilde{B}}$  vanish while transition current density is purely imaginary. In the presence of a magnetic field,  $\mathbf{j}_{\tilde{X},\tilde{X}}$  and  $\mathbf{j}_{\tilde{B},\tilde{B}}$  are nonzero and real-valued since the current density operator is Hermitian operator, while the transition current density  $\mathbf{j}_{\tilde{X},\tilde{B}}$  is complex-valued. When the magnetic field is perpendicular to the molecular plane, the real

part of  $\mathbf{j}_{\tilde{X},\tilde{B}}$  has ring current. In contrast, when the magnetic field is applied parallel to the molecule, the ring current is not present, i.e., the profile of current density is not a ring.

# References

- (S1) Becke, A. D. Density-Functional Exchange-Energy Approximation with Correct Asymptotic Behavior. *Phys. Rev. A* **1988**, *38*, 3098.
- (S2) Becke, A. D. Density-Functional Thermochemistry. III. The Role of Exact Exchange.

  J. Chem. Phys. 1993, 98, 5648.
- (S3) Lee, C.; Yang, W.; Parr, R. G. Development of the Colle-Salvetti Correlation-Energy Formula into a Functional of the Electron Density. *Phys. Rev. B* **1988**, *37*, 785.
- (S4) Miehlich, B.; Savin, A.; Stoll, H.; Preuss, H. Results Obtained with the Correlation Energy Density Functionals of Becke and Lee, Yang and Parr. Chem. Phys. Lett. 1989, 157, 200–206.
- (S5) Frisch, M. J.; Trucks, G. W.; Schlegel, H. B.; Scuseria, G. E.; Robb, M. A.; Cheeseman, J. R.; Scalmani, G.; Barone, V.; Petersson, G. A.; Nakatsuji, H.; Li, X.; Caricato, M.; Marenich, A. V.; Bloino, J.; Janesko, B. G.; Gomperts, R.; Mennucci, B.; Hratchian, H. P.; Ortiz, J. V.; Izmaylov, A. F.; Sonnenberg, J. L.; Williams-Young, D.; Ding, F.; Lipparini, F.; Egidi, F.; Goings, J.; Peng, B.; Petrone, A.; Henderson, T.; Ranasinghe, D.; Zakrzewski, V. G.; Gao, J.; Rega, N.; Zheng, G.; Liang, W.; Hada, M.; Ehara, M.; Toyota, K.; Fukuda, R.; Hasegawa, J.; Ishida, M.; Nakajima, T.; Honda, Y.; Kitao, O.; Nakai, H.; Vreven, T.; Throssell, K.; Montgomery, J. A., Jr.; Peralta, J. E.; Ogliaro, F.; Bearpark, M. J.; Heyd, J. J.; Brothers, E. N.; Kudin, K. N.; Staroverov, V. N.; Keith, T. A.; Kobayashi, R.; Normand, J.; Raghavachari, K.; Rendell, A. P.; Burant, J. C.; Iyengar, S. S.; Tomasi, J.; Cossi, M.; Millam, J. M.; Klene, M.; Adamo, C.; Cammi, R.; Ochterski, J. W.; Martin, R. L.; Morokuma, K.; Farkas, O.;

- Foresman, J. B.; Fox, D. J. Gaussian 16 Revision A.03. Gaussian Inc. Wallingford CT 2016.
- (S6) Williams-Young, D. B.; Petrone, A.; Sun, S.; Stetina, T. F.; Lestrange, P.; Hoyer, C. E.; Nascimento, D. R.; Koulias, L.; Wildman, A.; Kasper, J.; Goings, J. J.; Ding, F.; DePrince III, A. E.; Valeev, E. F.; Li, X. The Chronus Quantum (ChronusQ) Software Package. WIREs Comput. Mol. Sci. 2020, 10, e1436.
- (S7) Vallet, V.; Lan, Z.; Mahapatra, S.; Sobolewski, A. L.; Domcke, W. Photochemistry of pyrrole: Time-dependent quantum wave-packet description of the dynamics at the π 1 σ\*-S 0 conical intersections. J. Chem. Phys. 2005, 123, 144307.
- (S8) Atkins, P.; De Paula, J.; Friedman, R. *Physical chemistry: quanta, matter, and change*; Oxford University Press, USA, 2013.

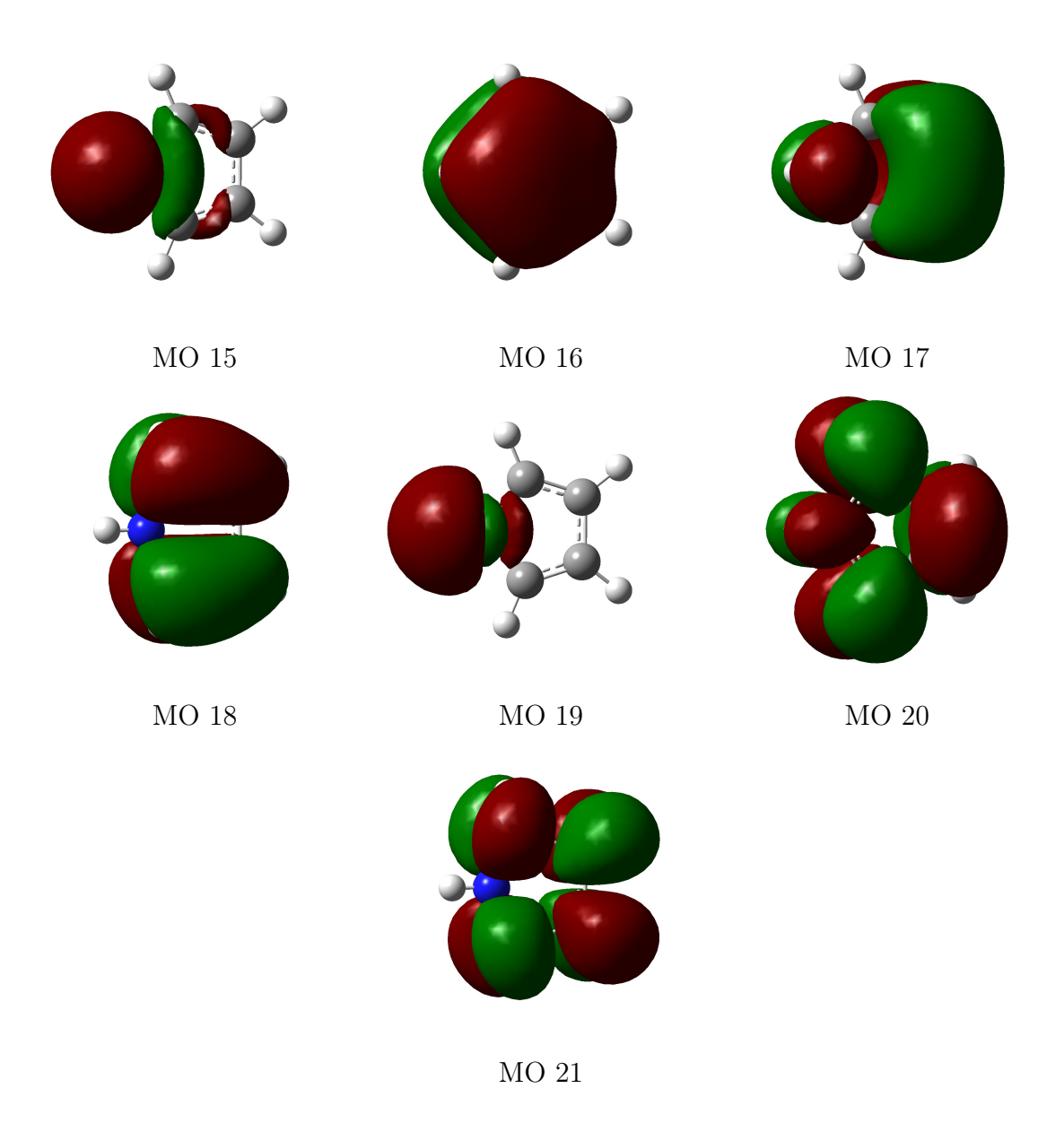


Figure S2. MO in the active space of CASSCF

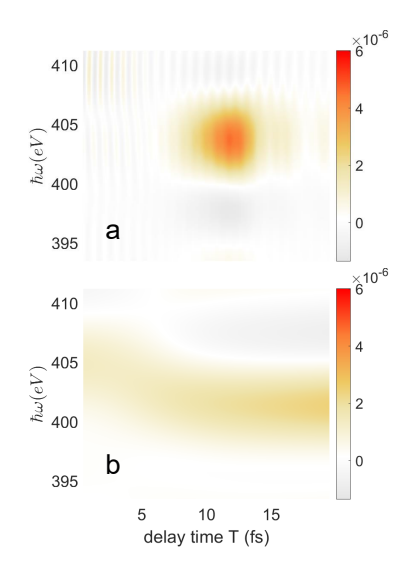
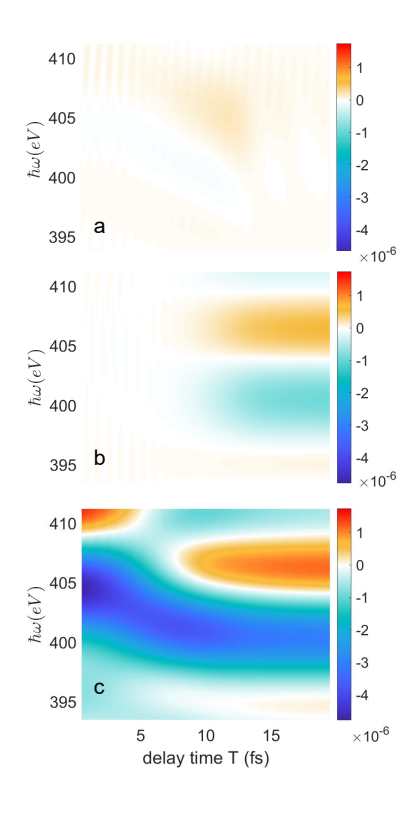
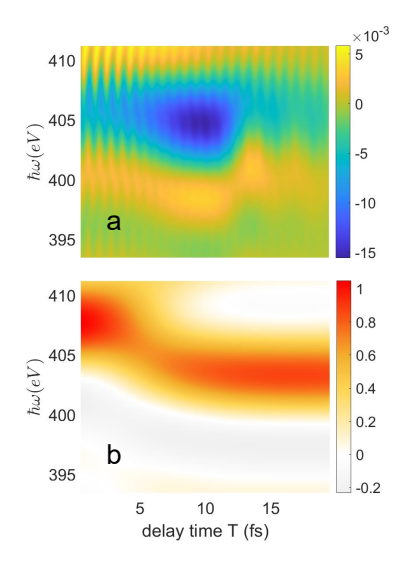


Figure S3. Separation of electronic state coherence and population in diabatic state basis of oriented molecule tr-XMCD spectrum with magnetic field in x. a: electronic state coherence contribution. b: electronic state population contribution.



**Figure S4.** Separation of electronic state coherence and population in diabatic state basis of oriented molecule tr-XMCD spectrum with magnetic field in y. a: electronic state coherence contribution. b:  $\tilde{X}$  electronic state population contribution. c:  $\tilde{B}$  electronic state population contribution.



**Figure S5.** Separation of coherence and population of rotationally-averaged transient absorption spectrum. a: electronic state coherence contribution. b: electronic state population contribution.

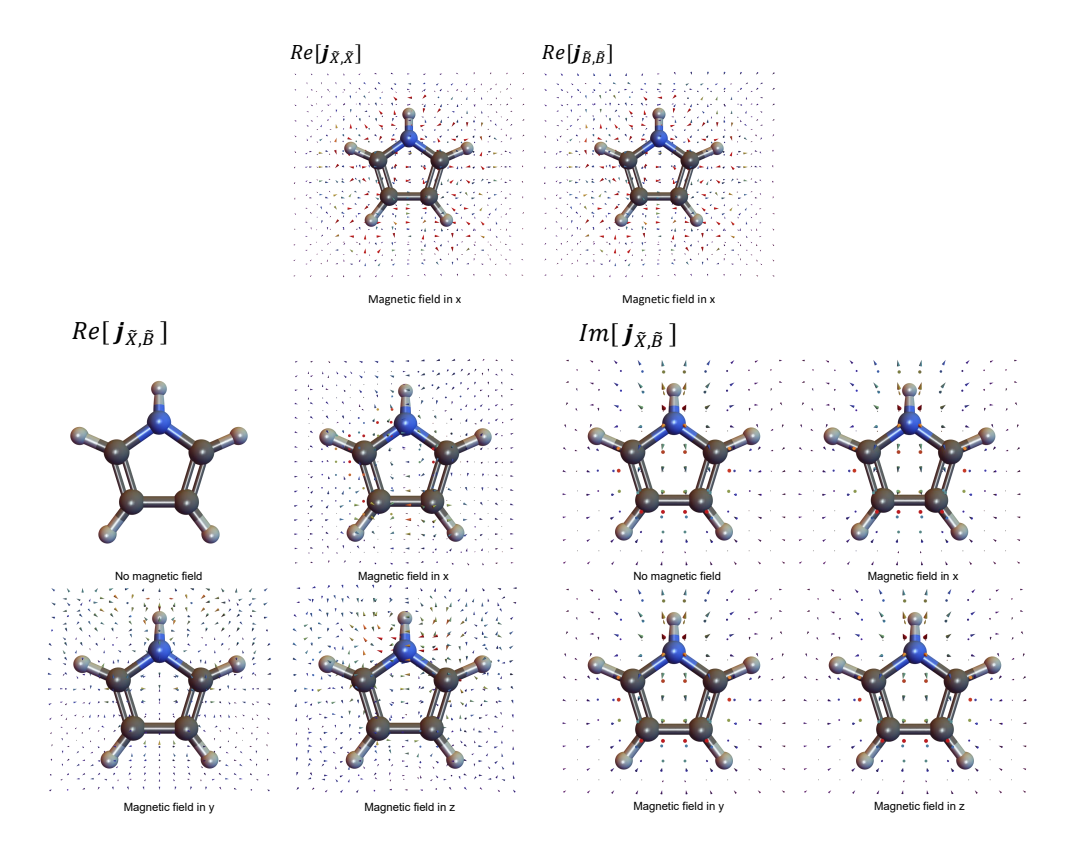


**Figure S6.** Upper panel: total tr-XMCD signal with rotational average. Lower panel: tr-XMCD signal with magnetic field applied in the  $x,\ y,\ z$  directions respectively.